

# Design and motion stability analysis of a straddle-type live working robot for power distribution lines

Shangkun Cheng<sup>a</sup>, Daozhu Wei<sup>a</sup>, Zhaowen Hu<sup>a</sup>, Hui Song<sup>a</sup>, Qi Chen<sup>a</sup>, Wei Wang<sup>a,\*</sup>

<sup>a</sup> \*School of Mechanical Engineering, Hefei University of Technology, Hefei 230009, China

## Abstract:

The motion stability of the live working robot on the cable is one of the factors affecting its work efficiency. Currently, most of the live working robots adopt a suspended structure, which makes it difficult to accurately position and clearly observe the condition of the cables. Additionally, stability analyses typically consider only the impact of the external loads, neglecting the influence of the cable stiffness variations on the robot's motion stability on the cable. This paper first designs a straddle-type live working robot structure and develops its control system, enabling it to safely and reliably perform live operations directly on the cable. Subsequently, an analysis of the robot's tipping stability during movement on the cable is conducted, and a dynamic model of the live working robot under three different cable stiffness conditions is established, identifying the factors affecting the robot's stability. Finally, through the construction of a simulation electric pole test bench, tests on motion control performance, tipping performance, and motion stability are designed. The data indicates that the control error of the robot is less than 6%, the minimum overturning angle range is between 29° and 32°, and the average Jerk is less than 2°/s<sup>3</sup>. These results are expected to lead to significant improvements in the field of live working robots.

**Keywords:** Power distribution lines. Design of straddle-type live working robot. Stability analysis. Straight cable. Inclined cable. Suspended chain state cable.

## 1. Introduction

Live working robot is a significant innovation in intelligent power maintenance, capable of assisting or replacing human workers in performing high-risk live-line tasks in complex electrical cable environments<sup>[1, 2]</sup>. However, the live working robot is typically suspended in mid-air, and the surrounding environment of the cables is highly variable. The robot must move along the cables with precision and stability without disrupting the power supply. As a result, the robot's motion stability on the cables becomes a key criterion for evaluating its performance.

The live working robot typically consists of the main body, drive unit, mobile unit and sensing unit. The existing live working robots are primarily suspended models, which rely on single or multiple wheel groups suspended on the cable to move. However, using a suspension-type robot has some limitations: due to the visual and position sensors mounted below the main body, accurate position localization and clear observation of the cable's condition are difficult<sup>[3-5]</sup>. To optimize these issues, we propose a straddle-type live working robot, which straddles the cable to offer a better view, allowing for direct observation of the cable's condition and completing tasks more safely and reliably.

The robot's motion stability refers to its ability to maintain balance and resist destabilization during tasks<sup>[6]</sup>. Currently, there are three main methods for analyzing the stability of live working robots: static and dynamic stability analysis method, sway frequency fitting method and dynamic modeling method. Static and dynamic stability analysis method mainly includes energy stability margin (ESM)<sup>[7-9]</sup>, force-angle stability margin (FASM)<sup>[10-13]</sup>, and zero-moment point (ZMP)<sup>[14-18]</sup>. For example, Qin Xinyan<sup>[19, 20]</sup> used FASM to analyze the stability of robots walking on the cable, and concluded that the robot remains stable even when the wind speed is 15.5 m/s. Dynamic and static stability analysis methods are more commonly applied in studies of wheel-legged robots on the ground. Given the unique operational environment of the live working robots, some scholars have also proposed a sway frequency fitting method, such as the one presented by Hong Zhan and Qian Jinju<sup>[21]</sup>,

<sup>22</sup>], which uses sinusoidal fitting based on the number of sign changes in swing angles within a fixed time period to calculate oscillation periods and frequencies. This method, however, has limitations in generalizability, especially when faced with non-periodic external loads. To accurately describe the dynamic characteristics of live working robots on cables, scholars have established the dynamic modeling method to analyze the robot's stability. Jiang Wei<sup>[23, 24]</sup>, for instance, used the Lagrange method to develop a dynamic model of the robot's balance system, proposing a wheel-based balance control method based on the conservation of angular momentum, which was verified through simulations. Alhassan<sup>[25]</sup> developed a suspended-type live working robot, using Lagrange's equation to derive the three-dimensional dynamic equations of the robot-cable coupling system and analyzed the response of the stability factors. Test results showed that the maximum vibration of the robot under external loads was 8% higher than without external loads. Lei Jin<sup>[26, 27]</sup> designed a flying-walking power line inspection robot and used a dynamic model to analyze how key factors such as the robot's speed and the pressure it exerts on the cable under external loads affect its stability, verifying the results through tests. However, these studies all focus on the stability of live working robots under external loads on cables. The difference in the stiffness of the cable itself is a limiting factor, affecting the robot's stability and operational efficiency.

To enhance the operational efficiency of live working robots and increase their working visibility on cables, we have designed a straddle-type live working robot structure. To address the issue of insufficient motion stability of the robot on cables caused by differences in cable stiffness, we established dynamic models for robot movement under three types of cable stiffness: straight cables, inclined cables, and catenary cables. Through experiments, we tested and analyzed the robot's motion control performance, overturning performance, and stability, verifying both the system's design and the accuracy of the theoretical analysis.

## 2. Robot Design Overview

### 2.1 Functional Requirements and Technical Specifications

Due to the unstructured and complex characteristics of high-altitude cables, the live working robot is influenced by factors such as constant gravitational fields, variable interface friction, and external disturbances. This results in significant unpredictability and time-varying characteristics of the external forces acting on the robot. Therefore, when the live working robot performs tasks in a flexible cable environment, the following aspects are particularly critical:

#### (1) Reliable Cable Gripping Ability

To ensure that the live working robot can flexibly operate on cables with different curvatures and diameters while safely and stably completing tasks, the robot must have a reliable gripping capability.

#### (2) Good Mobility

Safe movement on the cables is an essential premise for the live working robot to perform safe operations. The robot needs to demonstrate high stability when moving along the cable.

#### (3) Reliable Communication System

The live working robot must be equipped with a reliable communication system to report its operational status to the ground control center in real-time and receive commands. Additionally, the monitoring system should provide real-time feedback on the robot's position and status, ensuring that operators can effectively control and monitor the robot.

In addition to the above requirements, the robot's design should follow a modular design philosophy, with a compact size and a fully isolated mechanical and electrical structure. This allows for rapid replacement of structural components and operational devices, ensuring the robot can meet engineering and production needs.

## 2.2 Structure Design and Motion Analysis

### 2.2.1 Structure Design

In order to meet the requirements for a small volume, a compact size, and low center of gravity, the overall structure of the live working robot is symmetrically distributed on both sides, with its center of gravity located along the central axis, as shown in Figure 1. The main components include the cable gripping and movement device, control unit, intelligent perception unit, and frame. The cable gripping and movement device is designed as shown in Figure 1b. The gripping action is driven by a dual-axis lead screw motor that moves the traveling wheels and their motors in the X-direction (toward the cable), thus allowing the robot to grip the cable. The movement action occurs when the robot reaches the target position in the X-direction. The traveling wheel motor then drives the robot to move along the Y-axis (up or down along the cable), either advancing or retreating.

Considering the overall mass of the robot, the torque required by the movement motor must satisfy the following equation:

$$T = \frac{C \cdot mg \cdot R}{4 * N_i \mu} \quad (1)$$

Where: T is the torque required by the motor ( $N \cdot m$ ).C is the rolling friction coefficient between the wheel and the cable (0.1, based on tabulated values).m is the total mass of the robot (4.7 kg).g is the gravitational acceleration ( $9.8 \text{ m/s}^2$ ).R is the radius of the wheel (3 cm). $N_i$  is the reduction ratio of the gearbox (6). $\mu$  is the mechanical transmission efficiency (0.95)

By substituting the parameters into Equation (1), the required torque  $T=0.06N*m$ ;

To design the robot's maximum speed at 0.6 m/s, the motor's maximum rotational speed is calculated using the formula:

$$n = \frac{\vartheta \cdot 60 \cdot N_i}{2\pi R} \quad (2)$$

Where: n is the motor speed in rpm (rotations per minute).  $\vartheta$  is the robot's maximum speed (0.5 m/s).Substituting the parameters will give the motor speed n=400rpm.

The power required by the motor is calculated as:

$$P = \frac{T \cdot n}{9549} \quad (3)$$

Where: $P$  is the motor power required (kW).

Substituting the calculated torque and speed into Equation (3) will provide the required motor power  $P=0.003\text{KW}$ .

The intelligent perception unit consists of a picture transmission module and a stereo camera, as shown in Figure 1a and Figure 1c. The picture transmission module is connected to the top of the robot via a 360° rotating index plate and transmits real-time video signals from the site to the control center or operator's device. This enables real-time monitoring and evaluation of the working environment. The stereo camera uses parallax calculations to obtain depth information, providing the robot with 3D environmental data.

The robot is powered by two 12V 10,000mAh lithium battery packs, as shown in Figure 1d, and the weight of the battery pack helps lower the robot's center of gravity, contributing to overall body balance. All the robot's structural parts are made using 3D-printed resin materials, which are lightweight and highly flexible industrial-grade materials, ensuring the robot's overall structure is both lightweight and strong. The key technical parameters of the robot are listed in Table 1.

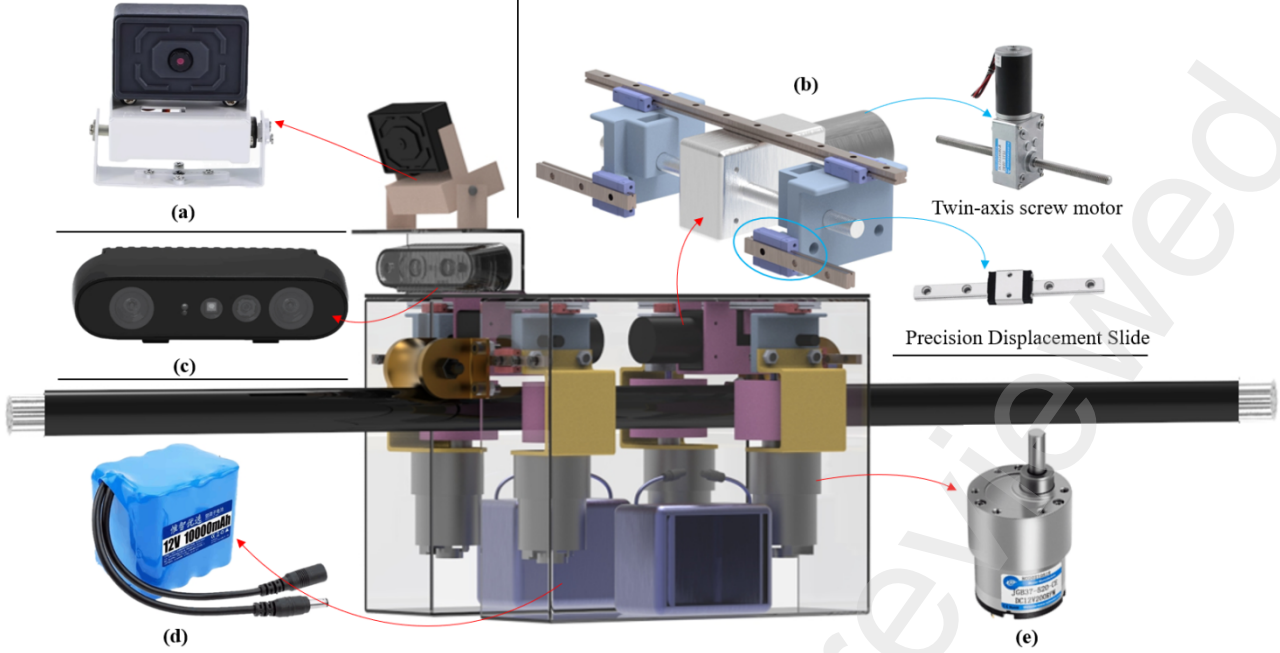


Figure 1. Overall structure of live working robot: (a) camera with picture transmission. (b) clamping travel device. (c) depth camera. (d) system power supply. (e) travel motor.

**Table 1.** Robot Parameter List

Categorization	Parameters
Mass/kg	4.7
Width/mm	180
Length/mm	200
Height/mm	214
Screw pitch/mm	1.25
Z direction expansion/mm	85
Rated torque of the screw motor/N*m	0.35
Rated torque of the traveling motor/N*m	0.06

### 2.2.2 Motion Analysis

To better control the robot's travel distance, we designed a travel distance control algorithm for the robot on the cable. It is assumed that the relationship between the number of pulses generated by the motor per revolution and the number of pulses generated by the motor per second can be expressed as:

$$P_s = n * \frac{N}{60} \quad (4)$$

Where:  $n$  is the motor speed, measured in pulses per second (PPS).  $P_s$  is the number of pulses generated by the motor per second.  $N$  is the number of pulses generated per revolution, corresponding to the motor's resolution.

When on a straight cable, the linear displacement corresponding to each pulse generated by the robot is:

$$d = \frac{2\pi r}{N} \quad (5)$$

Where:  $d$  is the linear displacement corresponding to each pulse.  $r$  is the radius of the clamped traveling wheel.

Therefore, the linear cable motion displacement  $L(P)$  corresponding to the accumulated  $P$  pulses is:

$$L(P) = P * \frac{2\pi r}{N} \quad (6)$$

However, when the robot moves along the catenary cable, the clamping wheel travels along the curved path of the cable. Therefore, we need to consider the curvature of the cable. The general shape of the cable can be described by the catenary

model, where the curvature at position  $x$  is denoted as  $k(x)$ , which is usually expressed as:

$$k(x) = \frac{d\theta}{ds} \quad (7)$$

Where:  $\theta$  is the angle between a tangent to the cable and a fixed direction,  $ds$  is the infinitesimal arc length element.

Considering the robot's motion along the cable, we integrate the arc length element  $ds$ , taking into account both the curvature and the tilt angle:

$$ds = \sqrt{(dx)^2 + (dy)^2} \quad (8)$$

For small curvature  $k(x)$ , this can be approximated as:

$$ds \approx \left(1 + \frac{1}{2}k(x)^2(dx)^2\right)dx \quad (9)$$

Considering both the tilt angle  $\alpha$  of the robot's movement along the cable and the curvature, the actual displacement  $dL$  in a small time interval  $dt$  is:

$$dL = r \cos \alpha \left(1 + \frac{1}{2}k(x)^2(dx)^2\right)dx \quad (10)$$

The cumulative actual displacement length  $L(t)$  can be obtained through integration:

$$L(t) = \int_0^t v(t) dt \quad (11)$$

Considering both the cable curvature and the tilt angle, the effective velocity is:

$$v = rw(t) \cos \alpha \left(1 + \frac{1}{2}k(x)^2\right) = \left(\frac{2\pi rn}{N}\right) \cos \alpha \left(1 + \frac{1}{2}k(x)^2\right) \quad (12)$$

The actual displacement length  $L(P)$ , combining the motor speed and the path corrected by the tilt angle and curvature factors, can be expressed as:

$$L(P) = \frac{2\pi r}{N} \cos \alpha \left(P + \int_0^P \frac{1}{2}k(x)^2 dP\right) \quad (13)$$

Based on equations (6) and (13), we adjust the control input voltage and pulse count of the movement motor to control the robot's movement, thus achieving the desired target position  $(x_i, y_i)$ .

### 2.3 Robot Hardware Design

To achieve compliant motion control for the live working robot and improve its operational accuracy and efficiency, Based on the functions provided by the robot, the entire robot hardware system is divided into three main parts: motion control, remote communication, and cable information collection.

**Motion Control:** The motion controller is the control execution end of the entire system. It is mainly responsible for receiving control commands from the remote monitoring terminal, and controlling the robot's clamping and movement actions, as well as the index plate of the image transmission module.

**Remote Communication:** The remote communication function uses a Lora wireless communication module (Manufacturer: Jixiang Technology, China; Model: TP1107), which supports multiple communication protocols, is highly sensitive, and consumes low power. It ensures stable, long-distance, and efficient communication in various complex environments. This module mainly receives motion control commands from the remote monitoring terminal and sends feedback on control effects and collected data.

**Cable Information Collection:** The cable information collection function utilizes an image transmission camera (Manufacturer: ZENCHANSI, China; Model: EWRF TS5823Pro) and a depth camera (Manufacturer: Orbbec, China; Model: Astra Pro Plus). These devices are mainly used to effectively capture the cable's surface condition and surrounding

environmental information. They ensure timely response to potential obstacles and changes during the robot's cable operation. The depth camera also provides real-time 3D depth data, which serves as the foundation for subsequent data analysis, processing, and positioning/navigation.

The robot is powered by two 12V lithium batteries. Since the robot needs to move along the cable and collect data during remote manual control, and remains in standby mode during the rest of the time, we designed a main switch circuit board to ensure the system's working hours. The main switch circuit board is controlled by the remote communication controller. Only when the switch is turned on, the entire motor movement system and cable information collection function can be powered on and activated. A schematic of the entire hardware system as shown in Figure 2.

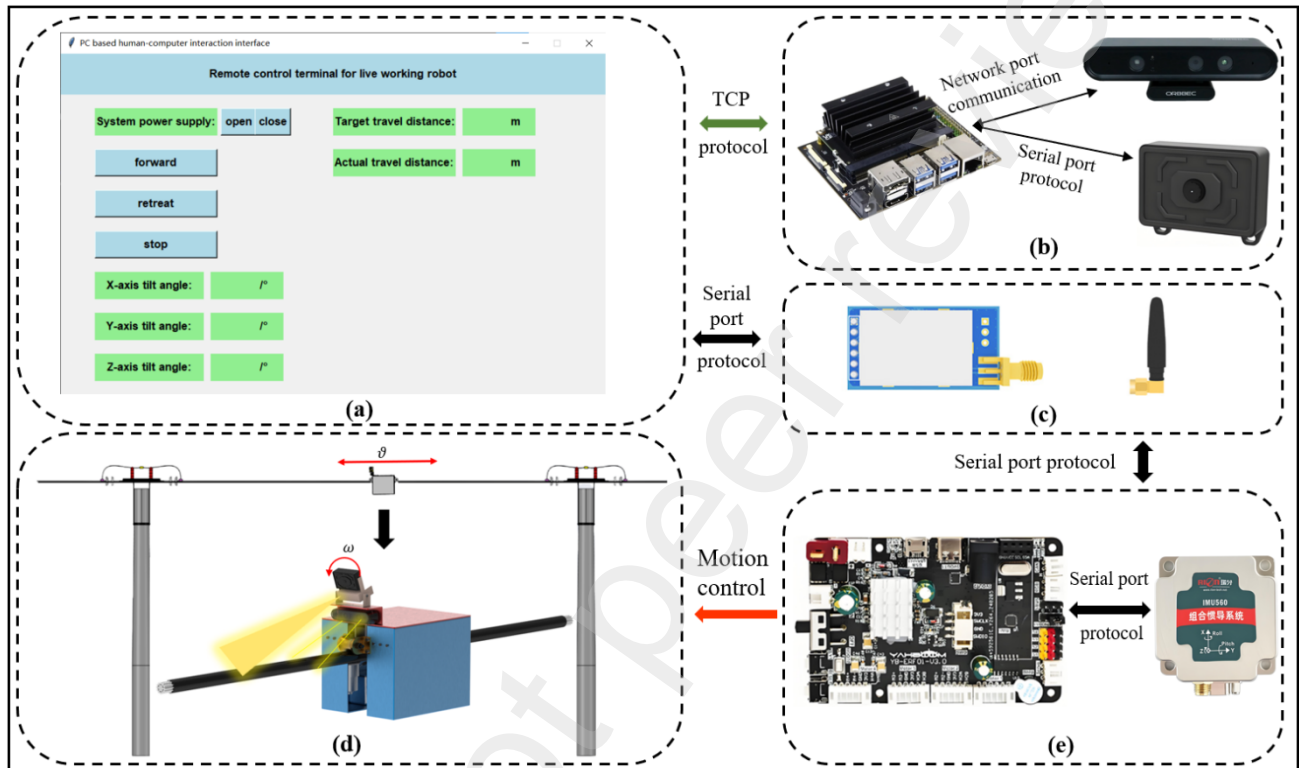


Figure 2. Schematic of the entire hardware system: (a) human-computer interactive page terminal. (b) upper computer. (c) Lora module. (d) robot cable motion. (e) motion control core and 9-Axis attitude sensor.

### 3 Motion Stability Analysis of Live Working Robots on Cables

#### 3.1 Stability analysis methods

When the robot moves along the cable, the cable often exhibits small irregularities due to manufacturing processes, as well as wear and deformation over long-term use. These factors cause the cable's operating surface to deviate from being strictly horizontal. Specifically, the direction of the contact force between the robot and the cable is not always aligned vertically upwards along the traveling wheel, leading to instability such as wobbling or tipping, which can affect the robot's motion stability. The angular acceleration ( $\alpha$ ) around the Y-axis directly reflects the extent of the robot's wobbling during movement.

In this study, we analyze the robot's movement stability in three typical cable conditions: straight cables, inclined cables, and catenary cables. A dynamic model is established to analyze the robot's motion in these scenarios, including the analysis of its angular acceleration ( $\alpha$ ) characteristics to identify key factors influencing motion stability.

Additionally, we introduce the concept of *Jerk*<sup>[28]</sup> (the rate of change of acceleration) to quantify variations in motion stability. *Jerk* represents how quickly acceleration changes during movement, and sudden changes in acceleration negatively impact stability. To summarize, *Jerk* and stability are negatively correlated, meaning that as *Jerk* increases, stability decreases.

$$Jerk = \frac{1}{T} \left| \frac{da(t)}{dt} \right| \Delta t \quad (14)$$

Before performing the dynamic modeling of the live working robot, it is important to note that it is a complex multi-rigid-body system. As a result, it is not easy to express all the inherent properties of the individual components in a dynamic model. Therefore, to solve the system's dynamic parameters without affecting the accuracy, we simplified the system's components to create an equivalent physical model. The following assumptions are made for the system:

- (1) The effect of the robot's weight on cable deformation is ignored during movement.
- (2) The friction coefficient at the contact points between the rollers and the cable is uniform.
- (3) The gravitational load is uniformly distributed across the contact surface between the cable and the rollers.
- (4) The robot's overall center of gravity remains on the robot's central axis, with no slippage occurring.

### 3.2 Tipping Stability Analysis of the Robot on the Cable

During the robot's movement, it is assumed that there is pure rolling constraint between the robot's wheels and the cable. The forces and torque exerted by the cable on the robot may cause tipping of the robot, or even the entire system. To analyze the stability of the system, we will use the force-angle stability criterion. First, we establish a ground reference coordinate system  $G$  and a robot body coordinate system  $S$ , as illustrated in Figure 3a. The robot's coordinate system  $S$  is rigidly fixed to the robot's body, with its origin located at the robot's center of gravity C. The position vector in the ground reference coordinate system is denoted as  $s^G p$ , and the position vectors of each wheel's contact point along the cable are denoted as  $i^G p$  and  $i^S p$  ( $i=1,2,3,4,5,6$ ).

In the ground reference coordinate system G, we assume that when the robot body oscillates, its attitude angle sequence around the  $xyz$  axes is  $[\alpha, \beta, \gamma]$ . Thus, the rotation matrix from the robot's body coordinate system S to the ground reference coordinate system G is given by:

$$R = \begin{bmatrix} \cos \beta \cos \gamma & \cos \sin \alpha \sin \beta - \sin \gamma \cos \alpha & \cos \sin \beta \cos \alpha + \sin \gamma \sin \alpha \\ \cos \beta \sin \gamma & \sin \alpha \sin \beta \sin \gamma + \cos \gamma \cos \alpha & \sin \gamma \sin \beta \cos \alpha - \cos \gamma \sin \alpha \\ -\sin \beta & \sin \alpha \cos \beta & \cos \gamma \cos \beta \end{bmatrix} \quad (15)$$

According to the force-angle stability criterion, in the robot's body coordinate system S, each contact point between the traveling wheels and the cable is sequentially connected, forming a closed supporting hexagon denoted as  $\hat{s^S a_i}$ . The pyramid formed by connecting the center of gravity C to the vertices of the supporting hexagon is called the stability cone, as shown in Figure 3b. Each edge of the supporting polygon is called the tipping axis, and when instability occurs, the robot body rotates around the tipping axis.

In the robot's body coordinate system S, the unit vector for each tipping axis is:

$$\hat{s^S a_i} = (p_{i+1} - p_i) / \|p_{i+1} - p_i\| \quad (16)$$

Considering the flexibility of the cable, its supporting polygon and the stability cone will also change accordingly in the ground coordinate system. In the ground coordinate system G, the unit vector of the tipping axis is:

$$\hat{G^S a_i} = R_S^G \hat{s^S a_i} \quad (i=1,2,3,4,5,6) \quad (17)$$

The perpendicular line from the center of gravity to the tipping axis is denoted as  $l$ :

$$l_i = \hat{O^G p_i} + (-\hat{O^G p_i} \cdot \hat{G^S a_i}) \cdot \hat{G^S a_i} \quad (18)$$

The projection of the equivalent gravitational force  $G$  onto the plane with  $\hat{G^S a_i}$  as its normal vector:

$${}^S\hat{G} = \hat{G} + (-\hat{G} \cdot {}_S^G R \hat{a}_i) \cdot {}_S^G R \hat{a}_i \quad (19)$$

The vector in the ground coordinate system is:

$${}^G\hat{G} = {}_S^G R (\hat{G} + (-\hat{G} \cdot {}_S^G R \hat{a}_i) \cdot {}_S^G R \hat{a}_i) \quad (20)$$

According to the force-angle stability criterion, we define the tipping angle of the robot's tipping axis is the angle  $\alpha_j$  which is between the projection  ${}^S\hat{G}$  of the equivalent gravity  $G$  and the perpendicular line  $l$ , as shown in Figure 3c:

$$\alpha_j = \begin{cases} \cos^{-1}(l_i \cdot {}^S\hat{G}) & (l_i \cdot {}^G\hat{G}) \cdot {}_S^G R \hat{a}_i > 0 \\ -\cos^{-1}(l_i \cdot {}^S\hat{G}) & (l_i \cdot {}^G\hat{G}) \cdot {}_S^G R \hat{a}_i \leq 0 \end{cases} \quad (21)$$

Similarly, the tipping angle  $\alpha_k$  at the foot support point is defined as the angle between the external force  $\hat{G}$  and the stability cone edge  $\widehat{O_S p_i}$ :

$$\alpha_k = \begin{cases} \cos^{-1}(\widehat{O_S p_i} \cdot \hat{G}) & (l_i \cdot {}_S^G R \hat{a}_i) \cdot {}_S^G R \hat{a}_i > 0 \text{ and } (l_{i+1} \cdot {}^G\hat{G}) \cdot {}_S^G R \hat{a}_i > 0 \\ -\cos^{-1}(\widehat{O_S p_i} \cdot \hat{G}) & (l_i \cdot {}_S^G R \hat{a}_i) \cdot {}_S^G R \hat{a}_i \leq 0 \text{ or } (l_{i+1} \cdot {}^G\hat{G}) \cdot {}_S^G R \hat{a}_i \leq 0 \end{cases} \quad (22)$$

The minimum tipping angle is:

$$T_{fasm} = \min_{j,k}(\alpha_j, \alpha_k) \quad (j,k=1,2,3,4,5,6) \quad (23)$$

Hence, it is concluded that the tipping stability angle of the live working robot is related to the system's structural parameters. The minimum tipping angle determines the robot's tendency to tip on the cable. A larger  $T_{fasm}$  indicates a smaller tendency for tipping. If  $T_{fasm}$  is less than 0, the robot cannot maintain balance. Using the data provided in Table 1, the minimum tipping angle when the tipping axis is defined by  $\hat{a}_2$  and  $\hat{a}_5$  is calculated to be  $31.71^\circ$ . This means that when the robot's left and right tilt angles are less than  $31.71^\circ$ , the robot will remain stable, while a tilt greater than  $31.71^\circ$  will cause noticeable tipping.

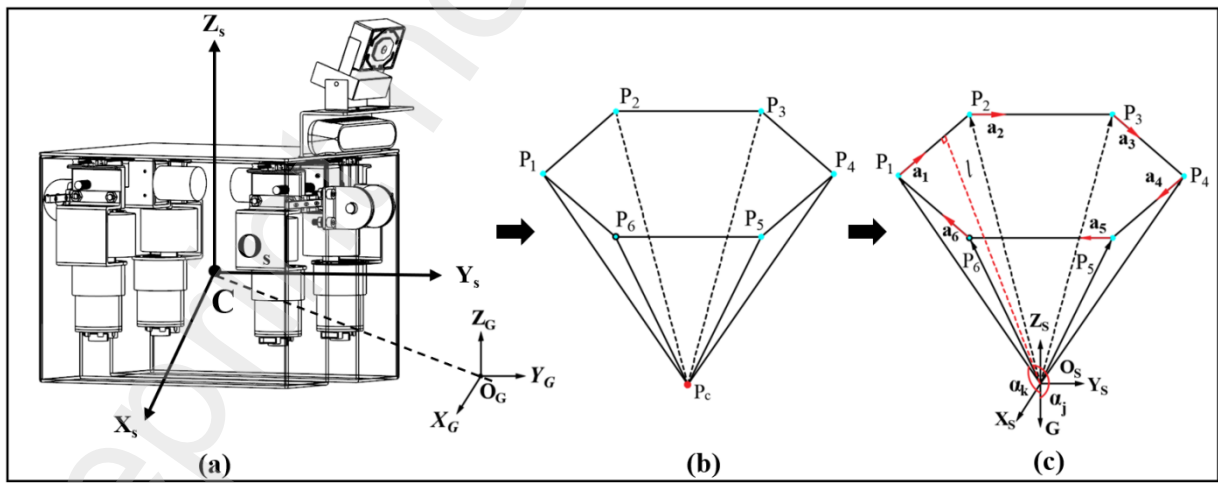


Figure 3. System stabilization cone

### 3.3 Analysis of the Impact of Straight Cables on the Robot's Motion Stability

When the robot moves along a straight cable, it generates a horizontal acceleration  $a$  and an angular acceleration  $\alpha$  that causes tilting around the X-axis. The force distribution is illustrated in Figure 4a. In the figure, the robot's lateral tipping angle is denoted as  $\theta$ , the robot's body weight is  $m$ , and the walking friction forces acting on the guide wheels A and F, as well as the respective friction forces preventing the robot from tilting, are  $f_{A1}$ ,  $f_{F1}$ ,  $f_{A2}$ , and  $f_{F2}$ , respectively, with the

corresponding normal support forces being  $F_{AN}$  and  $F_{FN}$ .

The frictional driving forces and the forces resisting tipping for the traveling wheels B, C, D, and E are represented by  $f_{B1}, f_{C1}, f_{D1}, f_{E1}, f_{B2}, f_{C2}, f_{D2}$ , and  $f_{E2}$ , with the corresponding normal support forces being  $F_{BN}$ ,  $F_{CN}$ ,  $F_{DN}$ , and  $F_{EN}$ .

A Cartesian coordinate system is established at the robot's center of gravity, allowing the robot's dynamic equation to be derived as follows:

$$\begin{cases} (F_{AN} + F_{FN}) \sin \theta + (f_{A2} + f_{F2}) \cos \theta + (f_{C1} + f_{E1} - f_{B1} - f_{D1}) \sin \theta = m\alpha l \\ f_{B2} + f_{C2} + f_{D2} + f_{E2} - f_{A1} - f_{F1} = ma \\ (F_{AN} + F_{FN}) \cos \theta - (f_{A2} + f_{F2}) \sin \theta + (f_{C1} + f_{E1} - f_{B1} - f_{D1}) \cos \theta = mg \\ mgl \cdot \sin \theta - (f_{C1} + f_{E1} + f_{B1} + f_{D1} + f_{A2} + f_{F2}) \cdot r = J\alpha \\ J = \frac{1}{12}m(w^2 + H^2) \end{cases} \quad (24)$$

The solution to equation (24) yields:

$$\alpha = \frac{mgl \sin \theta - (4F_C \sin \theta + mg)ur}{\frac{1}{12}m(w^2 + H^2)} \quad (25)$$

Where:  $F_C$  is the clamping force.  $u$  is the coefficient of friction.  $r$  is the wheel radius.  $w$  is the body width.  $H$  is the body height, and  $l$  is the distance from the top of the body to the cable.

Figure 4b shows the relationship between the robot's lateral tipping angle acceleration  $\alpha$ , the robot's lateral tipping angle  $\theta$ , and the clamping force  $F_C$  during straight motion. From the figure, it can be observed that the lateral tipping angle acceleration is negatively correlated with the clamping force and positively correlated with the lateral tipping angle. Increasing the clamping force can effectively reduce the lateral tipping angle acceleration, thereby improving the robot's stability.

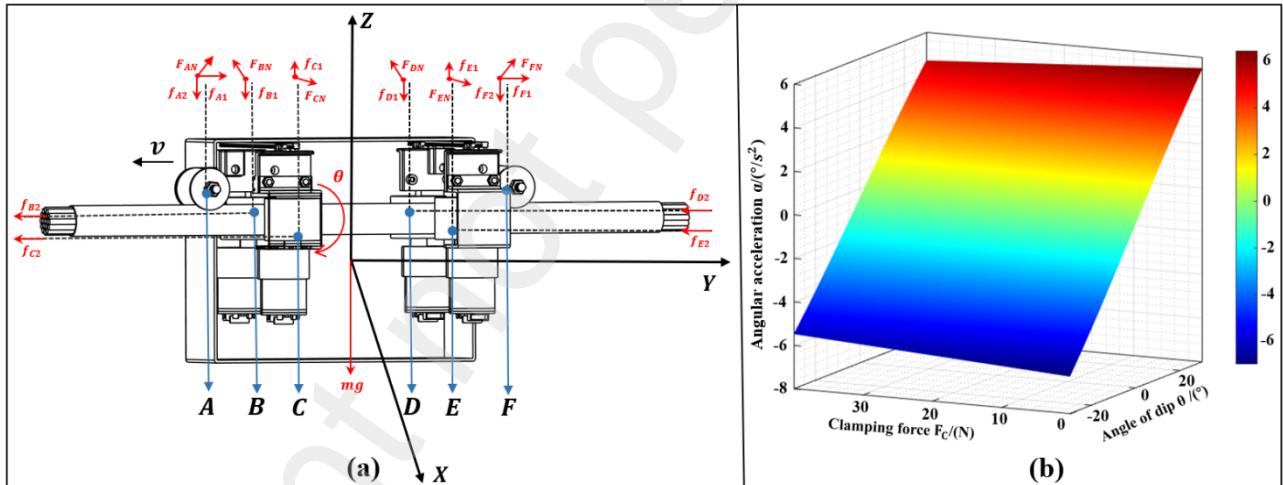


Figure 4. The impact of straight cables on the robot's motion stability: (a)analysis of the forces on the robot. (b) result analysis

### 3.4 Analysis of the Impact of Inclined Cables on the Robot's Motion Stability

When the robot moves on an inclined cable, the force distribution is shown in Figure 5a. In the figure, the angle between the cable and the horizontal direction is denoted as  $\varphi$ , and the robot's lateral tipping angle is  $\theta$ . Since the robot moves up or down the cable, only the direction of the frictional forces changes. Therefore, we performed a force analysis for the robot moving uphill along the cable. In the calculations, the positive and negative values of  $\varphi$  are considered. The robot's dynamic equation is:

$$\left\{ \begin{array}{l} (F_{CN} + F_{EN} - F_{BN} - F_{DN}) \cos \theta - (F_{AN} + F_{FN}) \sin \theta - (f_{c1} + f_{E1} - f_{B1} - f_{D1}) \sin \theta + (f_{A2} + f_{F2}) \cos \theta = 0 \\ (F_{CN} + F_{EN} - F_{BN} - F_{DN}) \sin \theta \sin \varphi + (F_{AN} + F_{FN}) \cos \theta \sin \varphi - (f_{B2} + f_{C2} + f_{D2} + f_{E2}) \sin \varphi \\ + (f_{c1} + f_{E1} - f_{B1} - f_{D1}) \cos \theta \sin \varphi - (f_{A2} + f_{F2}) \sin \theta \sin \varphi + (f_{A1} + f_{F1}) \sin \varphi = -ma \cos \varphi \\ (F_{CN} + F_{EN} - F_{BN} - F_{DN}) \sin \theta \cos \varphi + (F_{AN} + F_{FN}) \cos \theta \cos \varphi + (f_{B2} + f_{C2} + f_{D2} + f_{E2}) \cos \varphi \\ + (f_{c1} + f_{E1} - f_{B1} - f_{D1}) \cos \theta \cos \varphi - (f_{A2} + f_{F2}) \sin \theta \cos \varphi - (f_{A1} + f_{F1}) \cos \varphi - mg = ma \sin \varphi \\ mg \sin \varphi \cdot l \cdot \sin \theta - (f_{c1} + f_{E1} + f_{B1} + f_{D1} + f_{A2} + f_{F2})r = J\alpha \\ J = \frac{1}{12} m (w^2 + H^2) \end{array} \right. \quad (26)$$

The solution to equation (26) yields:

$$\alpha = \frac{mg \sin \varphi \cdot l \cdot \sin \theta - (4F_C \sin \theta + mg)ur}{\frac{1}{12} m (w^2 + H^2)} \quad (27)$$

Figures 5b-5e show the relationship between the robot's lateral tipping angle acceleration  $\alpha$ , the robot's lateral tipping angle  $\theta$ , the cable's inclination angle  $\varphi$ , and the clamping force  $F_C$  when the robot moves on an inclined cable. From the figures, it can be observed that the lateral tipping angle acceleration is positively correlated with the cable's inclination angle and the robot's lateral tipping angle. By increasing the clamping force, the lateral tipping angle acceleration can be effectively reduced.

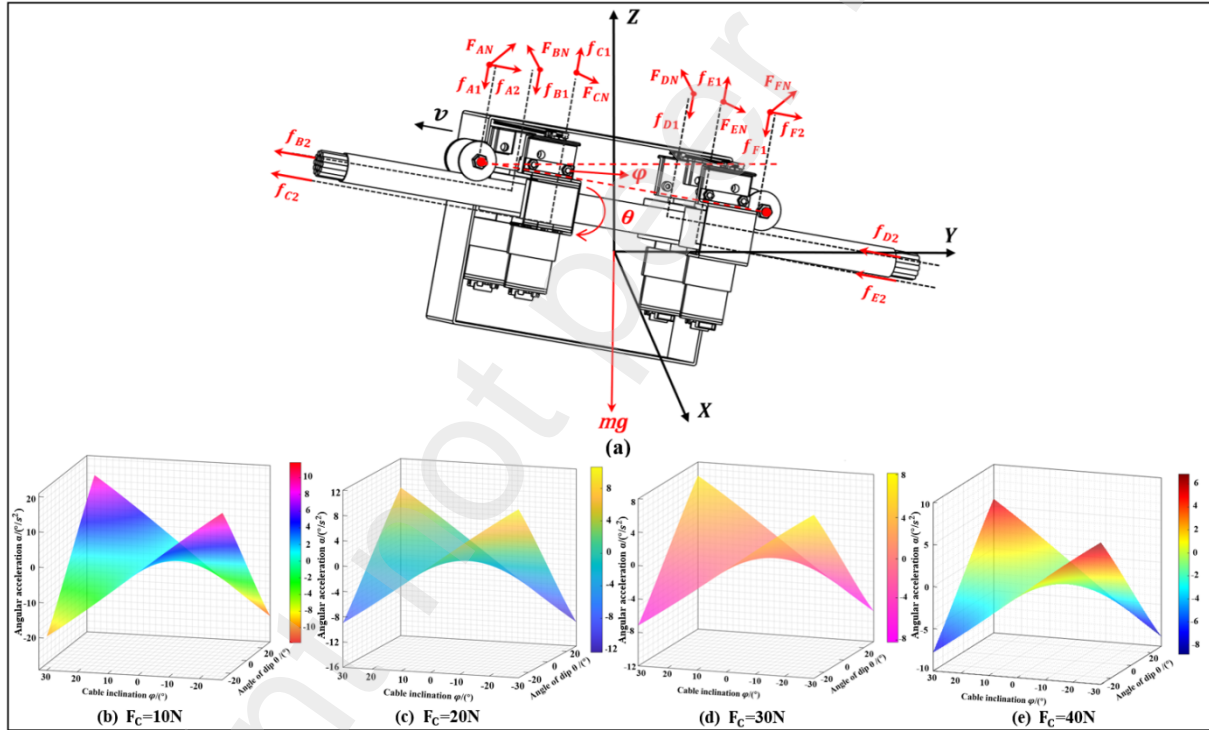


Figure 5. The impact of inclined cables on the robot's motion stability: (a) analysis of the forces on the robot. (b)-(e) results analysis

### 3.5 Analysis of the Impact of Catenary Cables on the Robot's Motion Stability

When the robot moves on a catenary cable, the force distribution is shown in Figure 6a. The angles between the guide wheels and the horizontal direction are denoted as  $\varphi$  and  $\gamma$ , the robot's lateral tipping angle is  $\theta$ , and the angle between the robot's body and the cable is  $\varepsilon$ . The robot's dynamic equation is:

$$\left\{ \begin{array}{l} (F_{CN} + F_{EN} - F_{BN} - F_{DN}) \cos \theta - (F_{AN} + F_{FN}) \sin \theta - (f_{c1} + f_{E1} - f_{B1} - f_{D1}) \sin \theta + (f_{A1} + f_{F1}) \cos \theta = 0 \\ (F_{CN} + F_{EN} - F_{BN} - F_{DN}) \sin \theta \sin \varepsilon + F_{AN} \cos \theta \sin \varphi + F_{FN} \cos \theta \sin \gamma - (f_{B2} + f_{c2} + f_{D2} + f_{E2}) \sin \varepsilon \\ + (f_{c1} + f_{E1} - f_{B1} - f_{D1}) \cos \theta \sin \varepsilon + f_{A2} \sin \varphi + f_{F2} \sin \gamma - f_{A1} \sin \theta \sin \varphi - f_{A1} \sin \theta \sin \gamma = -ma \cos \varepsilon \\ (F_{CN} + F_{EN} - F_{BN} - F_{DN}) \sin \theta \cos \varepsilon + F_{AN} \cos \theta \cos \varphi + F_{FN} \cos \theta \cos \gamma + (f_{B2} + f_{c2} + f_{D2} + f_{E2}) \cos \varepsilon \\ + (f_{c1} + f_{E1} - f_{B1} - f_{D1}) \cos \theta \cos \varepsilon - f_{A2} \cos \varphi - f_{F2} \cos \gamma - f_{A1} \sin \theta \cos \varphi - f_{A1} \sin \theta \cos \gamma - mg = ma \sin \varepsilon \\ mg \cos \varepsilon \cdot l \cdot \sin \theta - (f_{A2} + f_{F2} + f_{B1} + f_{c1} + f_{D1} + f_{E1})r = J\alpha \\ J = \frac{1}{12} m (w^2 + H^2) \end{array} \right. \quad (28)$$

On the catenary cable, the angular difference between the angles of the guide wheels A and F in the horizontal direction is:

$$\Delta\delta_1 = \varphi - \gamma = 2\arcsin\left(\frac{l_{AF}}{2R}\right) \quad (29)$$

The angular difference between the horizontal direction of guide wheel A and the horizontal direction of the robot's body is:

$$\Delta\delta_2 = \varphi - \varepsilon = 2\arcsin\left(\frac{l_{AB}}{2R}\right) \quad (30)$$

From equations (28), (29), and (30), the following can be obtained:

$$\alpha = \frac{mgl \sin \theta \left( \cos \varphi \cdot \left( 1 - 2\left(\frac{l_{AF}}{2R}\right)^2 \right) + \sin \varphi \cdot 2\left(\frac{l_{AB}}{2R}\right) \sqrt{1 - \left(\frac{l_{AB}}{2R}\right)^2} \right) - u(mg + 4F_C \cos \theta)r}{\frac{1}{12} m (w^2 + H^2)} \quad (31)$$

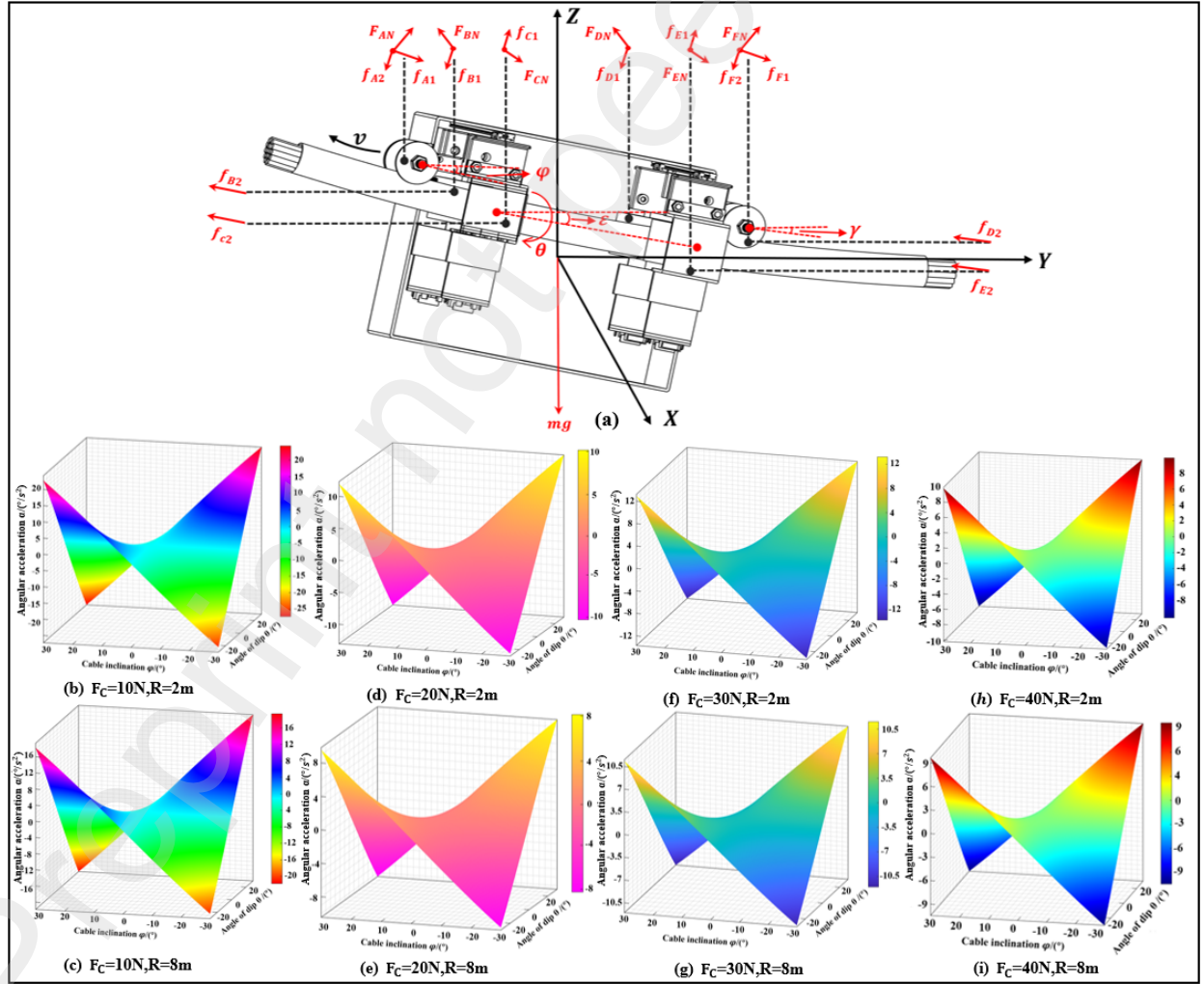


Figure 6. The impact of inclined cables on the robot's motion stability: (a) analysis of the forces on the robot. (b)-(i) results analysis

Figures 6b to Figures 6i show the relationship between the robot's lateral tipping angle acceleration  $\alpha$ , the robot's lateral tipping angle  $\theta$ , the cable's inclination angle  $\varphi$ , the clamping force  $F_C$ , and the cable radius R when the robot moves on a catenary cable. From the figures, it can be observed that the lateral tipping angle acceleration is positively correlated with the cable's inclination angle and the robot's lateral tipping angle, and negatively correlated with the clamping force  $F_C$  and the cable radius R.

## 4. Test and discussion

### 4.1 Test conditions

To verify the motion control characteristics of the robot designed in this study and the effectiveness of data collection on the cable, a simulation electric pole test bench was constructed, as shown in the figure. The height of the pole is adjustable between 1.8m and 2.5m, and the spacing between the poles can be adjusted from 2m to 2.5m. The live working robot is mounted on the cable, with its controller, data processing core, motor driver, and other components placed inside the robot's cabin, as shown in the figure. In August 2024, tests were designed and conducted to test the robot's motion control performance, tipping performance, and motion stability.

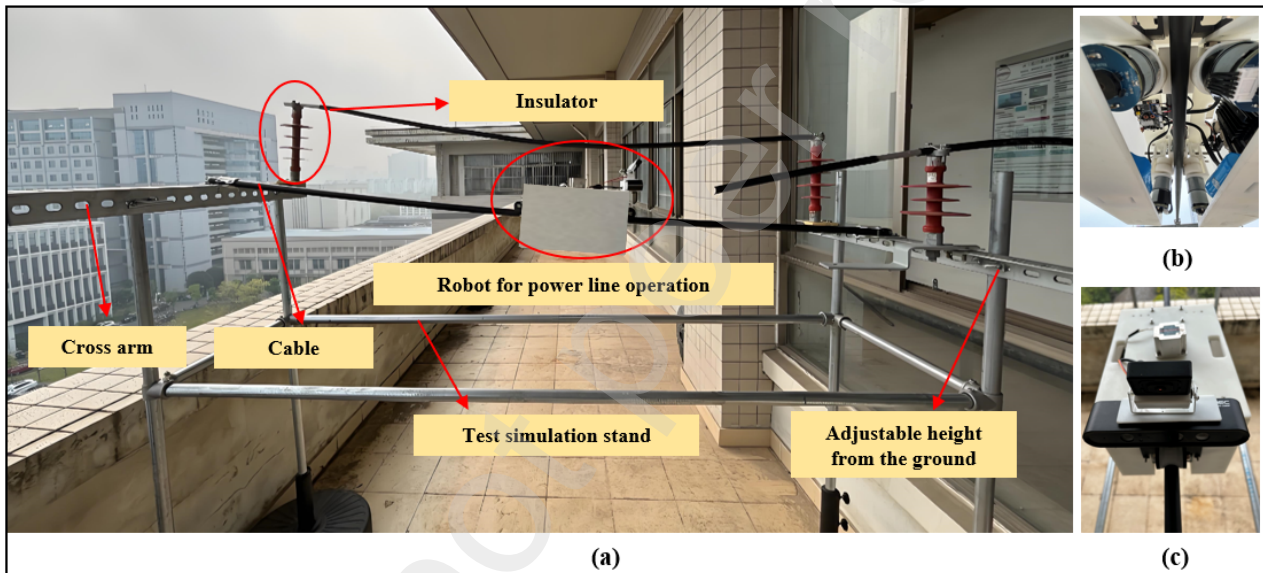


Figure 7. Test scenario: (a)the simulation electric pole test bench. (b)cabin interior layout. (c)robot exterior.

### 4.2 Robot motion control performance test

#### 4.2.1 Test methods

The control effect of the robot on the cable directly influences the quality of its live working operations. To ensure the controllability of the robot during live operations, motion control commands in the Y-direction were transmitted to the robot's motion controller via LoRa remote communication. The robot's motion control performance was evaluated through two sets of tests: the robot speed control test and the robot displacement control test.

In the robot speed control test, target speeds of 0.3 m/s, -0.5 m/s, and 0.2 m/s were sent to the robot, and the actual speed was recorded using response signals from a nine-axis attitude sensor. These signals were then output to a text file for documentation and analysis, allowing for the observation and evaluation of the robot's speed response characteristics.

In the robot displacement control test, three sets of target displacements (0.5 m, 1.0 m, and 1.5 m) were provided to the robot. The error between the target displacement and the actual displacement was measured through direct measurement techniques. During the test, the robot was maintained at a speed of 0.2 m/s, and each test was repeated five times to ensure the reliability of the results.

#### 4.2.2 The analysis of test results on robotic motion control performance

The results of the robot motion control performance test are shown in the figures. Figure 8a presents the results of the robot speed control test, which shows that under the step signal with target speeds ranging from -0.5 m/s to 0.3 m/s, the robot is able to move forward and backward on the cable. When the target speed is 0.3 m/s, the average error in the robot's actual speed is 0.022 m/s, with a maximum error of 0.15 m/s. When the target speed is -0.5 m/s, the average error in the actual speed is 0.027 m/s, with a maximum error of 0.24 m/s. When the target speed is 0.2 m/s, the average error is 0.010 m/s, with a maximum error of 0.12 m/s.

Figure 8b shows the results of the robot displacement control test. It can be seen that when the target displacement is 0.5 m, the average error in the robot's actual displacement is 0.032 m, with a maximum error of 0.07 m. When the target displacement is 1.0 m, the average error is 0.044 m, with a maximum error of 0.09 m. When the target displacement is 1.5 m, the average error is 0.046 m, with a maximum error of 0.08 m.

From the results of the above control tests, it can be concluded that the overall average error for speed control is within 6%, and the overall average error for displacement control is within 5%. These results indicate a high level of control accuracy, which is sufficient to meet the control requirements for cable-based operations of the live working robot.

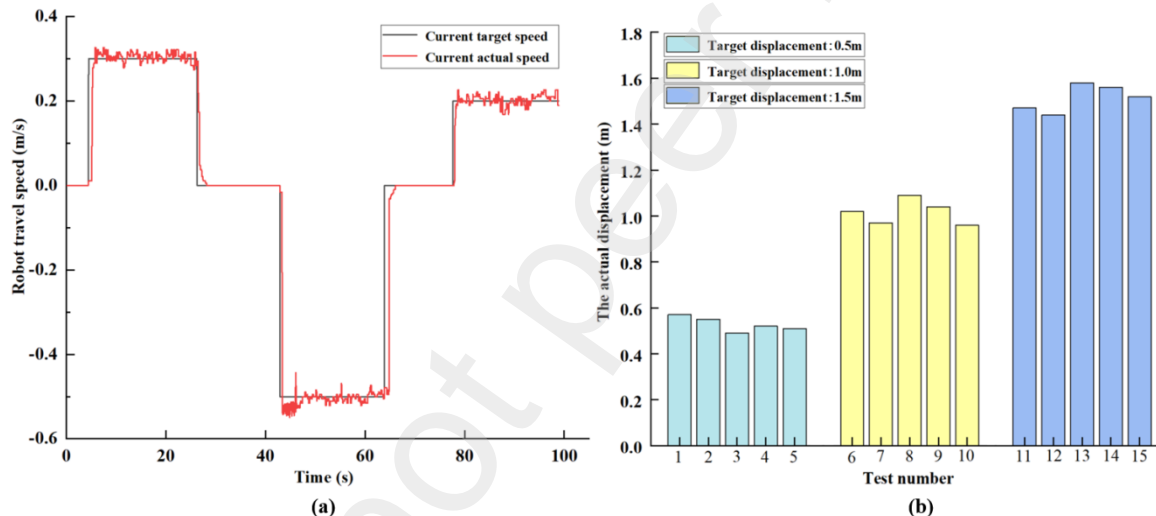


Figure 8. The test results on robotic motion control performance: (a) speed control test. (b) displacement control test.

#### 4.3 Robotic overturning performance test

##### 4.3.1 Test methods

To verify the minimum tipping angle range of the robot on the cable, we applied wind load to the robot's exterior. The robot's instability was captured in real-time using an i-SPEED high-speed camera (with a frame rate of 150,000 frames per second). The images captured by the camera were then converted to the HSV color space, and threshold values for the test bench and the robot's color were set. The tipping angle of the robot in the images was extracted. During the test, the robot remained stationary, with a clamping force set at 30 N. The test was repeated five times.

##### 4.3.2 Analysis of the test results for the robot's overturning range

By analyzing the image sequences captured by the high-speed camera, we were able to identify the critical angle at which the robot begins to lose stability. Figure 9 shows two randomly selected postures of the robot after significant instability during the test. The tipping angle of the robot was found to primarily range between  $29^\circ$  and  $32^\circ$ , with an average minimum tipping angle of  $30.2^\circ$ . The test results are in close agreement with the minimum tipping angle of  $31.71^\circ$  found in the previous tipping stability analysis.

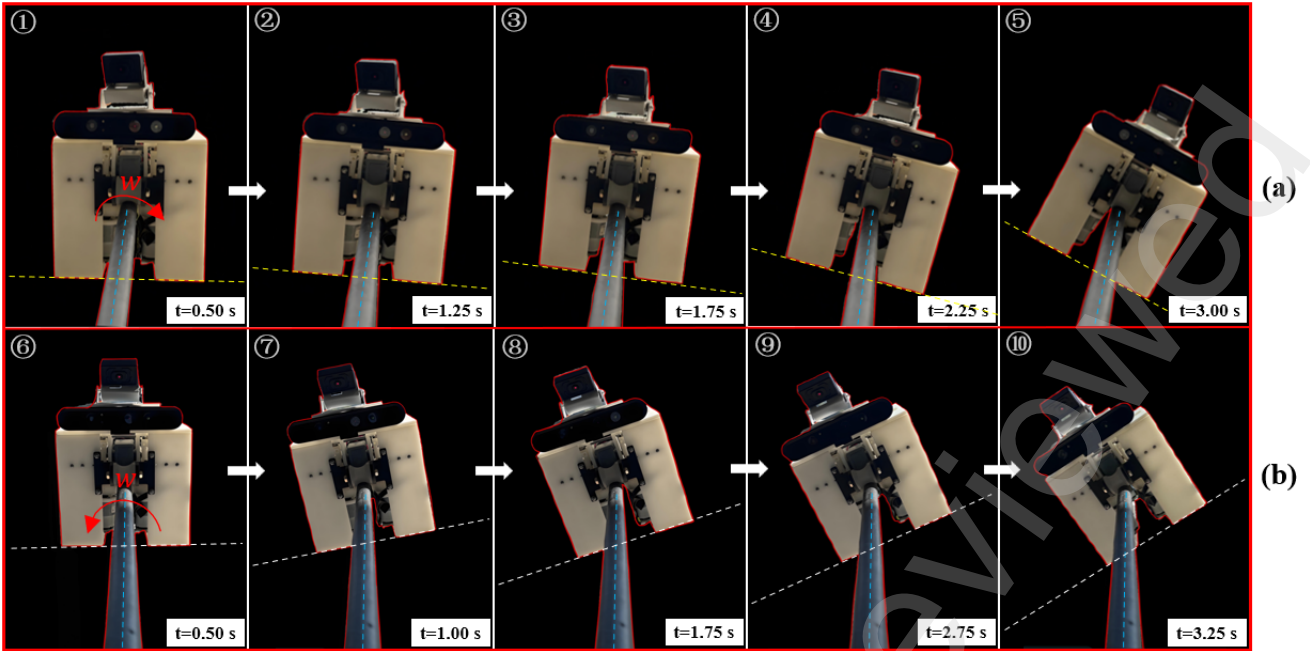


Figure 9. Robot posture.

#### 4.4 Test of robot motion stability performance

##### 4.4.1 Test methods

During the test, the robot was remotely controlled to move along the cable. A nine-axis attitude sensor mounted on the robot's body was used to monitor the robot's oscillation angle in real time. The response signals from the nine-axis attitude sensor were transmitted via the LoRa module on the controller and output to a text file for recording and storage. This allowed for the observation and evaluation of the sensor's response characteristics.

To verify the impact of the cable's shape on the robot's motion stability, we set up seven test conditions and conducted robot motion stability performance tests. Each condition was repeated three times :

(1) Straight cable, as shown in Figure 10b:

Condition 1: The robot speed was set to 0.5 m/s, with the cable's inclination set to 0°. We tested the robot's angular acceleration change rate with three clamping forces (15 N, 25 N, 35 N).

(2) Inclined cable, as shown in Figure 10a:

Condition 2: The robot speed was set to 0.5 m/s, with a clamping force of 30 N. We tested the angular acceleration change rate of the robot moving uphill along the cable at three different cable inclination angles (4°, 8°, 12°).

Condition 3: The robot speed was set to 0.5 m/s, with a clamping force of 30 N. We tested the angular acceleration change rate of the robot moving downhill along the cable at three different cable inclination angles (4°, 8°, 12°).

Condition 4: The robot speed was set to 0.5 m/s, with a cable inclination angle of 4°. We tested the angular acceleration change rate of the robot moving uphill along the cable at three different clamping forces (15 N, 25 N, 35 N).

Condition 5: The robot speed was set to 0.5 m/s, with a cable inclination angle of 4°. We tested the angular acceleration change rate of the robot moving downhill along the cable at three different clamping forces (15 N, 25 N, 35 N).

(3) Suspended chain state cable, as shown in Figure 10c:

Condition 6: The robot speed was set to 0.5 m/s, with a clamping force of 30 N. The pre-tension of the cable was adjusted, and we tested the angular acceleration change rate of the robot with different values of R(8m,15m,20m).

Condition 7: The robot speed was set to 0.5m/s, with a fixed pre-tension between the cables. We tested the angular acceleration change rate of the robot with three different clamping forces (15 N, 25 N, 35 N).

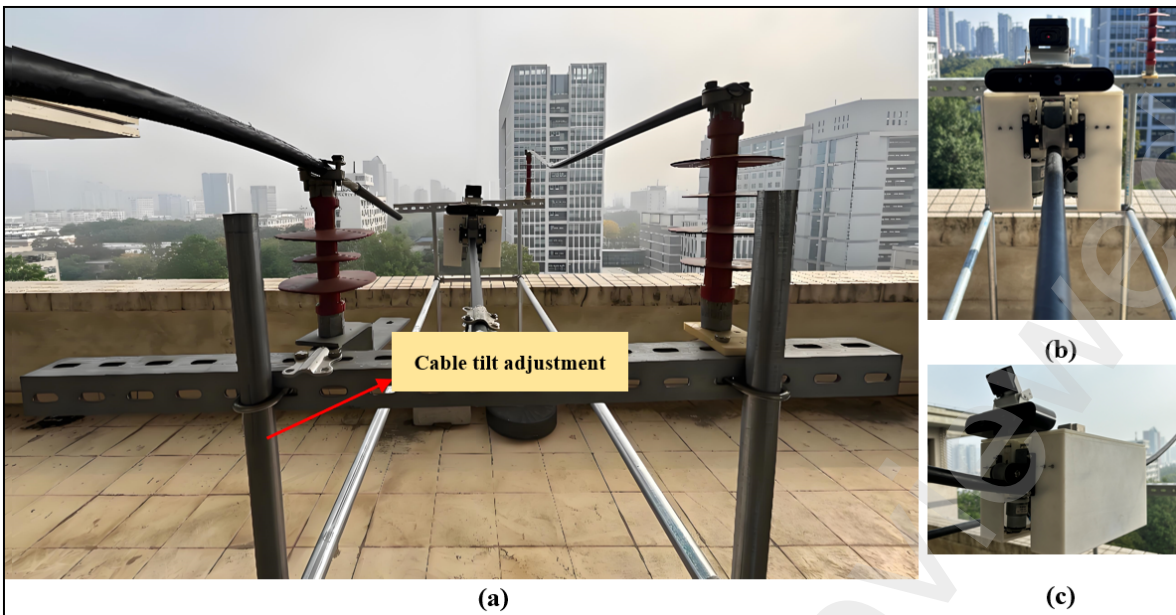


Figure 10. Robot motion stability performance test scenario: (a) inclined cable. (b) straight line cable. (c) suspended chain state cable.

#### 4.4.2 Analysis of the testing results for the robot's motion stability performance

The results of the robot motion stability performance test are shown in Figure 11. The corresponding robot angular acceleration curves under different operating conditions are shown in Figure 11a to- Figure 11g. The maximum lateral tilt angular accelerations for each condition are as follows:  $-5.895^{\circ}/s^2$ ,  $-7.821^{\circ}/s^2$ ,  $7.912^{\circ}/s^2$ ,  $8.148^{\circ}/s^2$ ,  $11.217^{\circ}/s^2$ ,  $7.329^{\circ}/s^2$ ,  $9.718^{\circ}/s^2$ , and  $9.975^{\circ}/s^2$ . Figure 11h illustrates the average angular acceleration for each test condition. From Equation (14), the corresponding average *Jerk* (impact rate) for the robot under each condition is as follows:  $1.33^{\circ}/s^3$ ,  $1.5016^{\circ}/s^2$ ,  $1.4672^{\circ}/s^2$ ,  $1.5912^{\circ}/s^2$ ,  $1.686^{\circ}/s^2$ ,  $1.9764^{\circ}/s^2$ , and  $1.87^{\circ}/s^2$ .

It can be concluded that the stability of the live working robot is better in a straight cable environment compared to an inclined cable or a catenary cable. When the clamping force is the same, the robot exhibits better stability in the inclined cable environment compared to the catenary cable, with the overall average *Jerk* values being quite similar across all conditions.

It can be concluded from Figure 11h that in a straight cable environment, increasing the clamping force reduces the lateral tilt angular acceleration. In an inclined cable environment, when the clamping force is held constant, an increase in the cable inclination angle leads to an increase in lateral tilt angular acceleration. When the cable inclination angle is the same, increasing the clamping force can reduce the lateral tilt angular acceleration. In the suspended chain state cable environment, when the clamping force is constant, an increase in the curvature radius of the suspended cable results in a decrease in lateral tilt angular acceleration. When the curvature radius of the suspended cable is the same, increasing the clamping force can effectively reduce the lateral tilt angular acceleration.

The test results are consistent with the conclusions derived from the analysis of stability influences, indicating that the live working robot designed in this study possesses good motion stability performance.

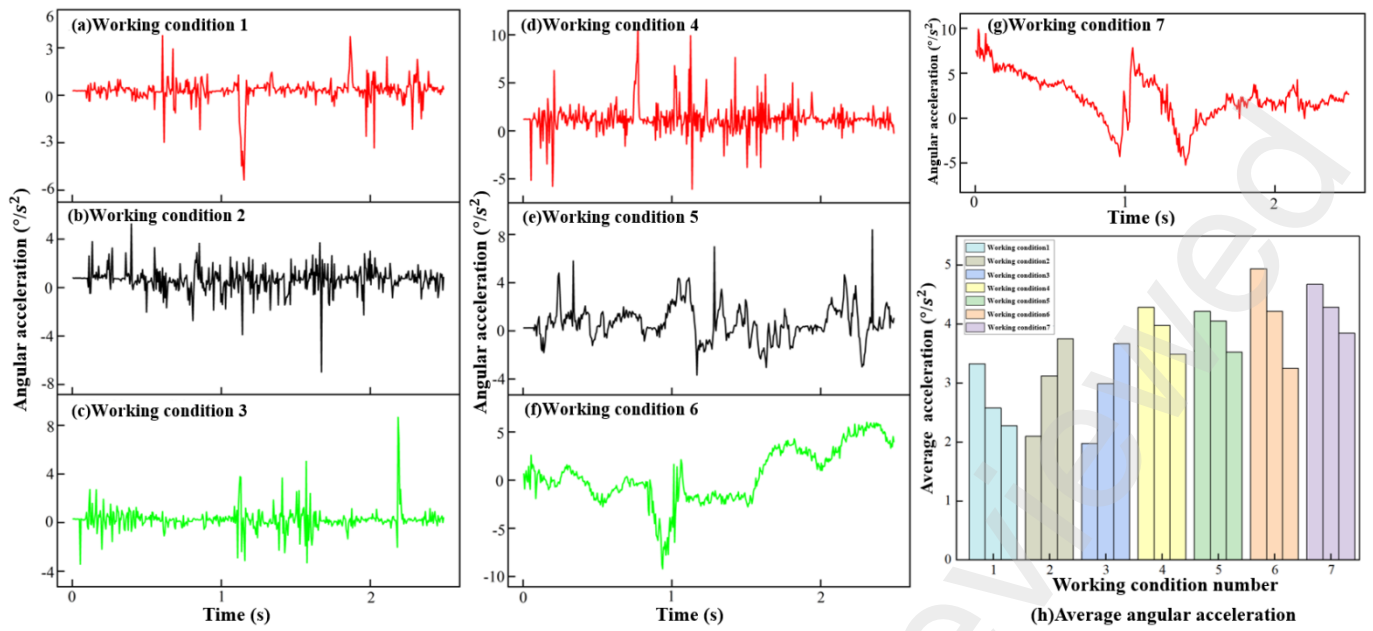


Figure 11. The results of the robot motion stability performance test.

#### 4.5 Discussion

This study designs a straddle-type live working robot, establishes a dynamical model for the robot's movement along the cable, and analyzes the factors affecting the stability of the robot. Through simulated bench tests, the motion control performance, tipping performance, and the motion stability on the cable of the robot under three typical operational conditions have been validated. Most existing literatures [3-5] discussing live working robots do not mention their control precision. In contrast, the robot designed in this study features a hardware control system design with control precision of less than 6%, allowing for accurate movement along the cable.

According to the literatures [23,24], scholars have conducted stability control studies on live working robots, but only simulation validation was performed. In contrast, this study not only carried out a dynamical analysis but also set up a simulated electric pole test bench. By using a nine-axis attitude angle sensor to record the robot's angular velocity in real-time, a more objective understanding of its stability performance was obtained. Similarly, the literatures [19,20] utilized the force-angle stability criterion to assess the tilting stability of live working robots. However, this study offers a more accurate and intuitive observation of the designed robot's tipping performance by capturing its instability state with a high-speed camera during the simulated power pole tests.

To validate the superiority of the live working robot designed in this study, image processing was conducted to analyze its motion posture in three different environments, as shown in the figure. Figures 12a, 12b, and 12c respectively represent the robot's motion postures on a straight cable, an inclined cable, and a catenary cable. From the figures, it can be observed that within the same time frame, the robot's motion on the straight cable is relatively stable, with a minimum tilt angle of  $1.9^{\circ}$  and a maximum tilt angle of  $6.2^{\circ}$ . In the case of the inclined cable, the minimum and maximum tilt angles were  $2.4^{\circ}$  and  $8.7^{\circ}$ , respectively. For the motion on the catenary cable, the minimum tilt angle was  $3.9^{\circ}$  and the maximum tilt angle was  $12.4^{\circ}$ . All these angles are less than the minimum tilting angle, and the test data demonstrate that the live working robot designed in this study exhibits good motion stability performance.

To sum up, this study addresses the stability issues faced by live working robots due to the inherent irregularities of the cables. Theoretical analysis and test validation of the robot's stability under cables with varying stiffness were conducted, providing new insights for the development and stability performance design of live working robots.

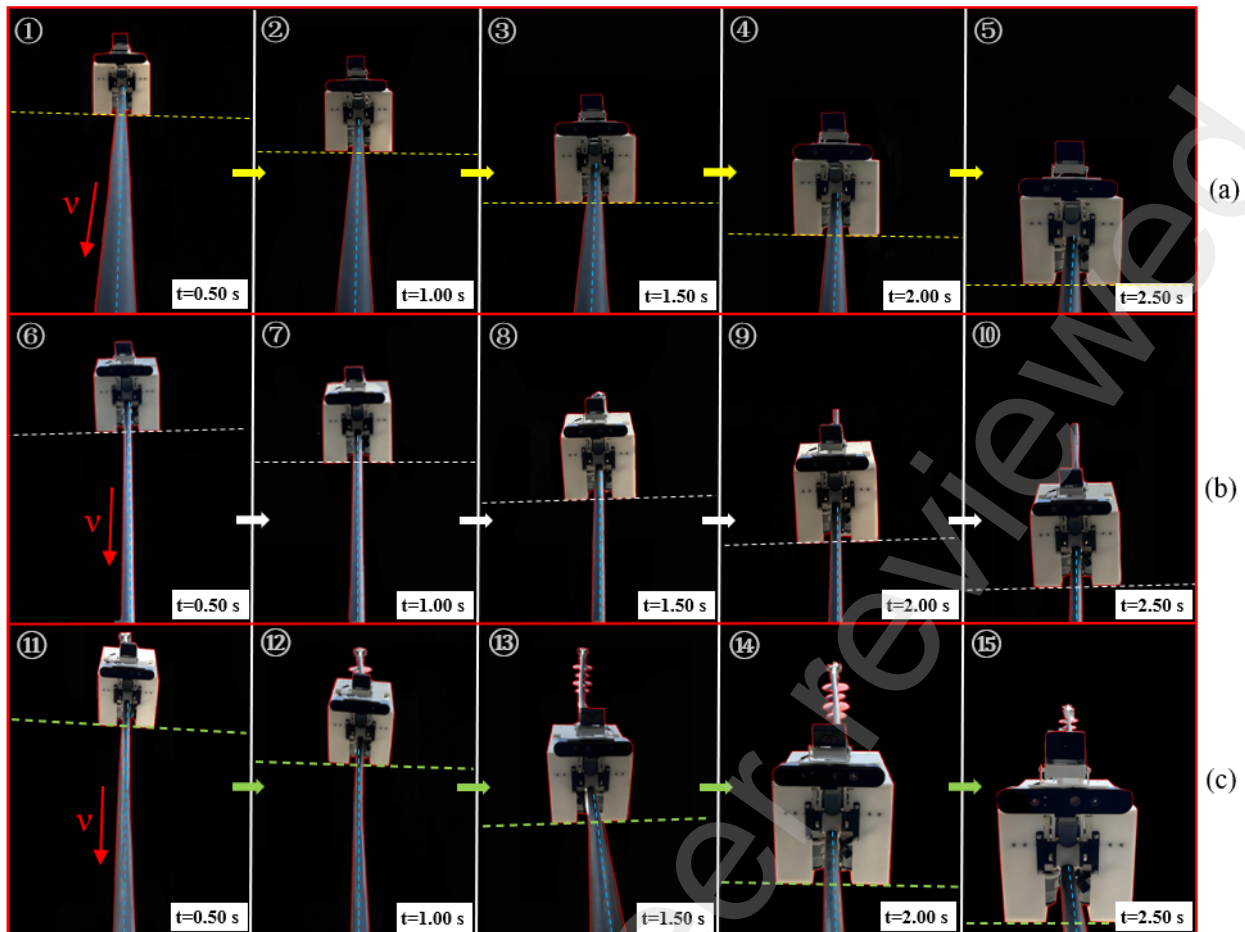


Figure 12. Robot motion posture: (a) robot in straight line cable. (b) robot in inclined cable. (c) robot in suspended chain state cable.

## 5. Conclusion

To address the challenges of accurate position localization and clear observation of cable conditions faced by suspended live working robots, we designed a straddle-type live working robot structure. This robot is capable of straddling on the cable, allowing for direct observation of the cable's status. Through simulated electric pole bench tests, it was demonstrated that the overall average error for speed control of the robot remains within 6%, and the overall average error for displacement control stays within 5%. In terms of tipping performance, the robot's minimum tilting angle ranges from  $29^\circ$  to  $32^\circ$ . Regarding motion stability performance, the average jerk values in each operational condition were measured as follows:  $1.33^\circ/\text{s}^3$ ,  $1.5016^\circ/\text{s}^3$ ,  $1.4672^\circ/\text{s}^3$ ,  $1.5912^\circ/\text{s}^3$ ,  $1.686^\circ/\text{s}^3$ ,  $1.9764^\circ/\text{s}^3$ , and  $1.87^\circ/\text{s}^3$ . The results indicate that the straddle-type live working robot structure designed in this study exhibits good stability, providing new insights for the development and stability performance design of live working robots.

## CRediT authorship contribution statement

**Shangkun Cheng:** Data curation, Formal analysis, Software, Validation, Writing – original draft, Writing – review & editing. **Wei Wang:** Funding acquisition, Investigation, Methodology. **Daozhu Wei:** Investigation, Methodology, Software. **Zhaowen Hu:** Investigation, Methodology. **Hui Song:** Funding acquisition, Resources. **Qi Chen:** Investigation, Methodology.

## Acknowledgements

This study is supported by the Electric Power Research Institute of China Grid Anhui Electric Power Co., (Grant No. B3120524002J).

## Declaration of Competing Interest

The authors declare that they have no known competing financial interests or personal relationships that could have

appeared to influence the work reported in this paper.

## Data availability

Data will be made available on request.

## References

- [1] CHEN Y T, WANG Y H, TANG X M, et al. Intelligent power distribution live-line operation robot systems based on stereo camera [J]. *High Volt*, 2023, 8(6): 1306-18, doi:10.1049/hve2.12349.
- [2] FU Q, GUAN Y, ZHU H. A Novel Robot with rolling and climbing modes for power transmission line inspection [J]. *2022 IEEE/RSJ International Conference on Intelligent Robots and Systems (IROS)*, 2022: 7122-8, doi:10.1109/IROS47612.2022.9981434.
- [3] EKREN N, KARAGÖZ Z, SAHIN M. A review of line suspended inspection robots for power transmission lines [J]. *J Electr Eng Technol*, 2024, 19(4): 2549-83, doi:10.1007/s42835-023-01713-7.
- [4] ALHASSAN A B, ZHANG X D, SHEN H M, et al. Power transmission line inspection robots: A review, trends and challenges for future research [J]. *Int J Electr Power Energy Syst*, 2020, 118: 19, doi: 10.1016/j.ijepes.2020.105862.
- [5] KUCUK Z K, EKREN N, SAHIN M. Review of power transmission line inspection robots moving on ground wire [J]. *2022 International Conference on Engineering and Emerging Technologies (ICEET)*, 2022: 1-6, doi: 10.1109/ICEET56468.2022.10006846.
- [6] BAO H M, ZHANG Y, SONG M P, et al. A review of underwater vehicle motion stability [J]. *Ocean Eng*, 2023, 287: 30, doi: 10.1016/j.oceaneng.2023.115735.
- [7] BRUNNER M, FIOLKA T, SCHULZ D, et al. Design and comparative evaluation of an iterative contact point estimation method for static stability estimation of mobile actively reconfigurable robots [J]. *Robot Auton Syst*, 2015, 63: 89-107, doi: 10.1016/j.robot.2014.09.003.
- [8] RYU S, WON J, SEO T. Simulation study on four-wheeled mobile robot mechanisms using various performance criteria [J]. *Robot Auton Syst*, 2024, 179: 10, doi: 10.1016/j.robot.2024.104749.
- [9] CHEN D, LU S, LUO X, et al. Stability analysis of a mobile health care robot [J]. *2016 IEEE International Conference on Real-Time Computing and Robotics (RCAR) Proceedings*, 2016: 591-6, doi: 10.1109/RCAR.2016.7784096.
- [10] YOU B, SHI S D, CHEN C, et al. Contact force optimization to enhance fault-tolerant motion stability of a hexapod robot [J]. *J Bionic Eng*, 2024, 21(5): 2199-214, doi: 10.1007/s42235-024-00577-5.
- [11] ZHANG L Z, ZHA F S, GUO W, et al. Heavy-duty hexapod robot sideline tipping judgment and recovery [J]. *Robotica*, 2024, 42(5): 1403-19, doi: 10.1017/S0263574724000274.
- [12] LIU J S, LIU J G, XUE Z H, et al. Research on stability of modular multi-legged robots with non-isomorphic configurations [J]. *Trans Inst Meas Control*, 2024: 13, doi: 10.1177/01423312241288043.
- [13] ZHAO J B, ZHANG J Q, LIU H Z, et al. Path planning for a tracked robot traversing uneven terrains based on tip-over stability [J]. *Asian J Control*, 2023, 25(5): 3569-83, doi: 10.1002/asjc.3048.
- [14] HALDAR A I, PAGAR N D. Predictive control of zero moment point (ZMP) for terrain robot kinematics [J]. *Mater Today, Proc (Netherlands)*, 2023: 122-7, doi: 10.1016/j.matpr.2022.10.286.
- [15] VAN DER NOOT N, BARREA A. Zero-Moment Point on a bipedal robot under bio-inspired walking control [J]. *MELECON 2014 - 2014 17th IEEE Mediterranean Electrotechnical Conference*, 2014: 85-90, doi: 10.1109/MELCON.2014.6820512.
- [16] ANDO T, WATARI T, KIKUUWE R. Reference ZMP generation for teleoperated bipedal robots walking on Non-Flat Terrains [J]. *Proceedings of the 2021 IEEE/SICE International Symposium on System Integration (SII)*, 2021: 794-800, doi: 10.1109/IEEECONF49454.2021.9382614.
- [17] JAELYOUNG J, JAE UK C, JONG-HYEON P. Foot placement method to change velocity of running biped robot [J]. *2015 15th International Conference on Control, Automation and Systems (ICCAS)*, 2015: 79-84, doi: 10.1109/ICCAS.2015.7364882.
- [18] TAMURA K, KAWAMURA A. Robust and high-mobility walking control for uneven terrain without zero-moment-point feedback [J]. *2017 IEEE International Conference on Industrial Technology (ICIT) Proceedings*, 2017: 866-71, doi: 10.1109/ICIT.2017.7915473.
- [19] QIN X Y, LI H D, FENG T M, et al. Hybrid control method of multimode switching for flying-walking power-line

- inspection robots [J]. CAAI Transactions on Intelligent Systems. 2023, 18(06): 1243-58, doi: 10.11992/tis.202211011.
- [20] LI H D. Research on multi-mode switching control of hybrid system of flying-walking power robot [D]. Shihezi University, CN, 2023, doi: 10.27332/d.cnki.gshzu.2023.000119.
- [21] QIAN J J, WU G P, PENG X Y, et al. Technology for gesture detection and job control of inspection robot for overhead transmission line under wind load [J]. Guangdong Electric Power. 2017, 30(01): 116-20, ISSN :1007-290X.
- [22] HONG Z ,WU G P ,WANG W, et al. Attitude detection and operation optimization of inspection robot under wind load [J]. Machinery Design & Manufacture, 2016, (12): 197-200, ISSN : 1001-3997.
- [23] JIANG W, DAI W H, et al. Robust stabilization control of live working robot under wind load based on angular momentum conservation principle [J]. Proc Inst Mech Eng Part C-J Eng Mech Eng Sci, 2023, 237(22): NP1-NP , doi: 10.1177/09544062231157946.
- [24] JIANG W, ZOU D H, MA S B, et al. Dynamic walking characteristics and control of four-wheel mobile robot on ultra-high voltage multi-split transmission line [J]. Trans Inst Meas Control, 2022, 44(6): 1309-22, doi: 10.1177/01423312211043001.
- [25] ALHASSAN A B, ZHANG X D, SHEN H M, et al. Investigation of aerodynamic stability of a lightweight dual-arm power transmission line inspection robot under the influence of wind [J]. Math Probl Eng, 2019, 2019: 16, doi: 10.1155/2019/2139462.
- [26] QIN X Y, JIA B, LEI J, et al. A novel flying-walking power line inspection robot and stability analysis hanging on the line under wind loads [J]. Mech Sci, 2022, 13(1): 257-73, doi: 10.5194/ms-13-257-2022.
- [27] JIE Z, JIN L, XINYAN Q, et al. Modeling and analysis of a flying-walking power line inspection robot [J]. CCRIS'21: 2021 2nd International Conference on Control, Robotics and Intelligent System, 2021: 25-30, doi: 10.1145/3483845.3483850.
- [28] LIN M M. Research on the stability evaluation of robotic arm for robot training [D]. ZheJiang University, CN, 2022, doi: 10.27461/d.cnki.gzjdx.2022.002255.

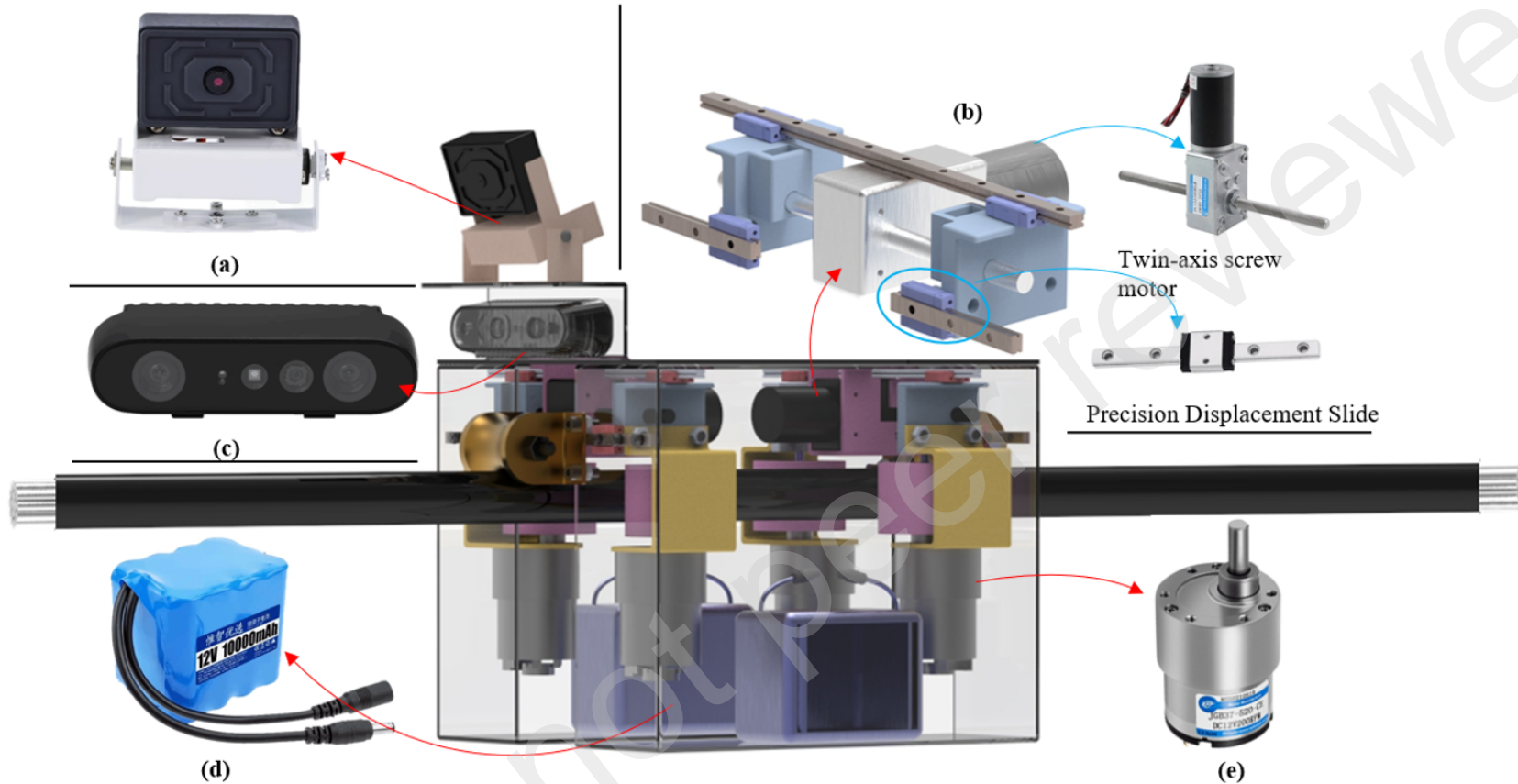


Figure 1. Overall structure of live working robot: (a) camera with picture transmission. (b) clamping travel device. (c) depth camera. (d) system power supply. (e) travel motor.

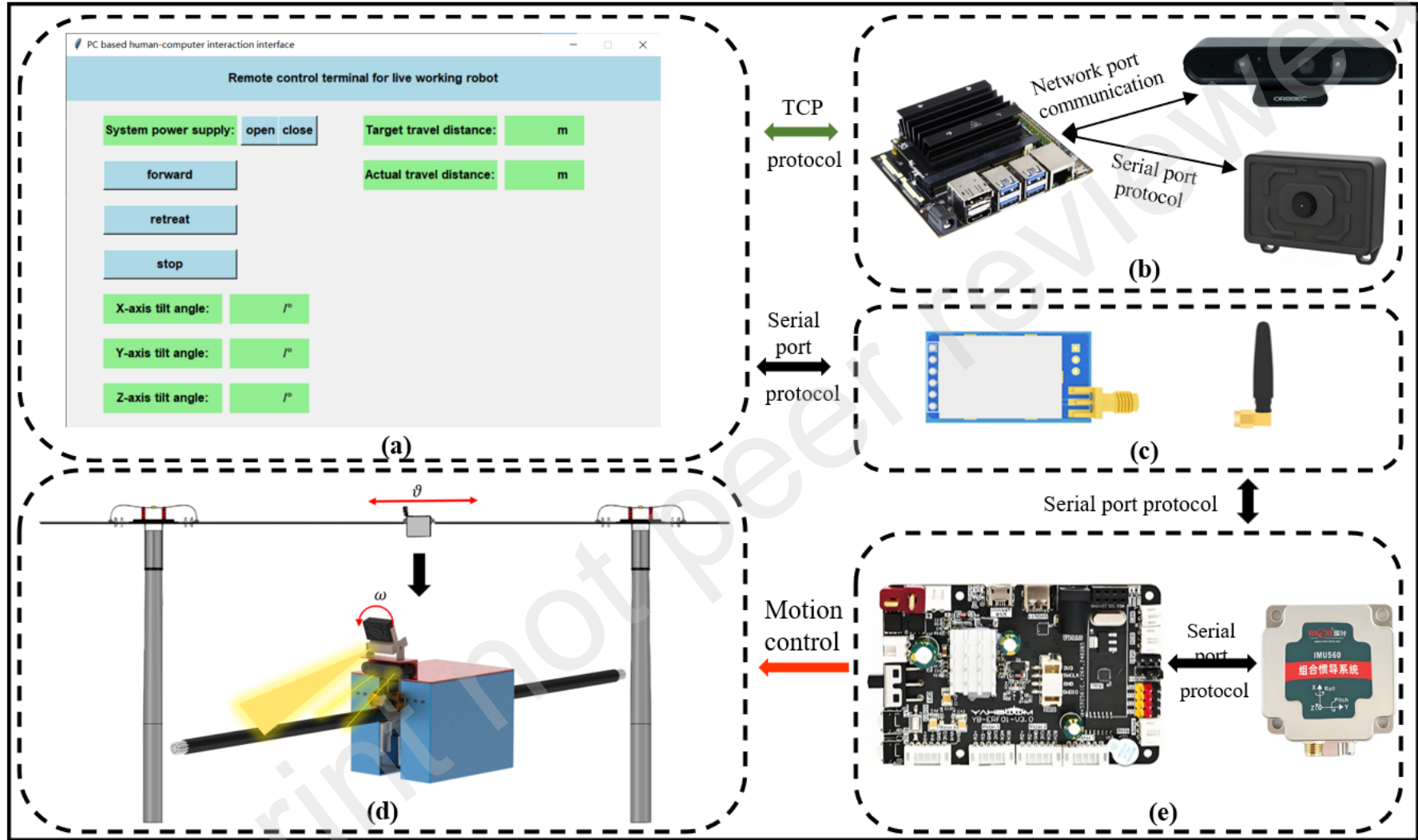


Figure 2. Schematic of the entire hardware system: (a) human-computer interactive page terminal. (b) upper computer. (c) Lora module. (d) robot cable motion. (e) motion control core and 9-Axis attitude sensor.

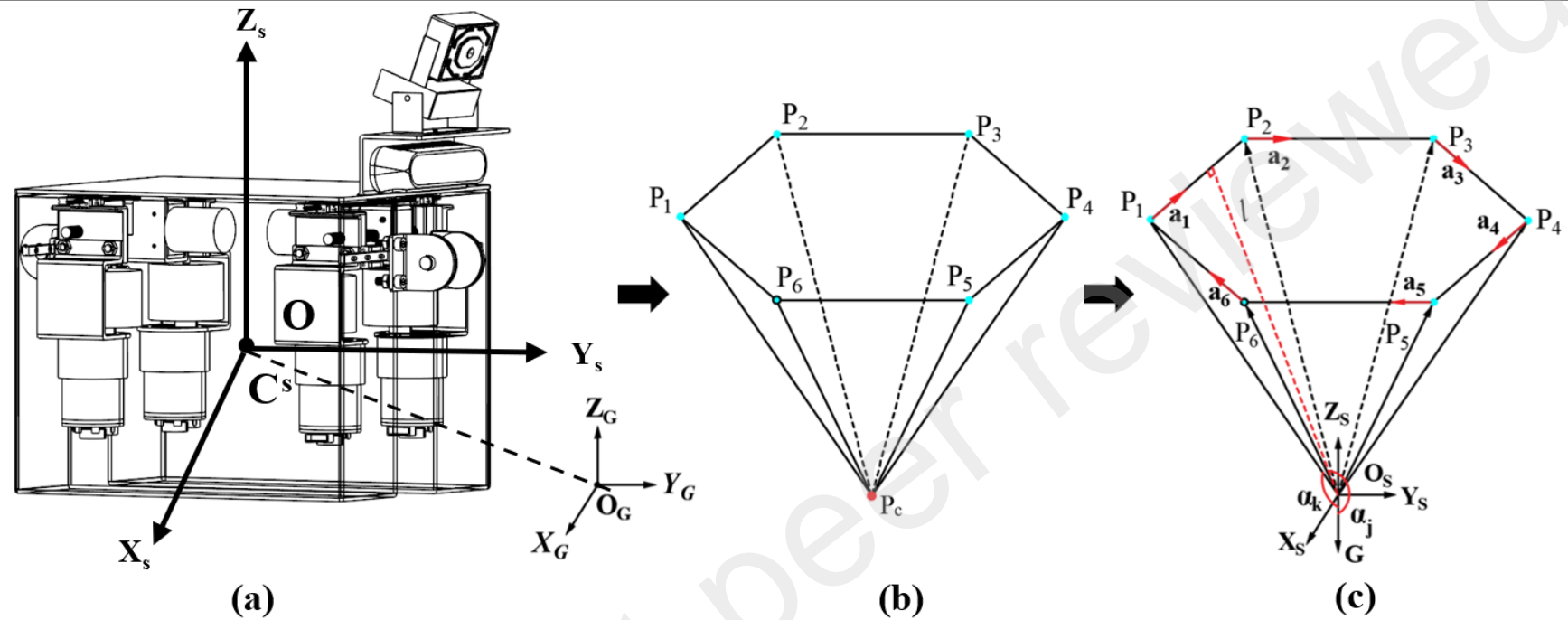


Figure 3. System stabilization cone

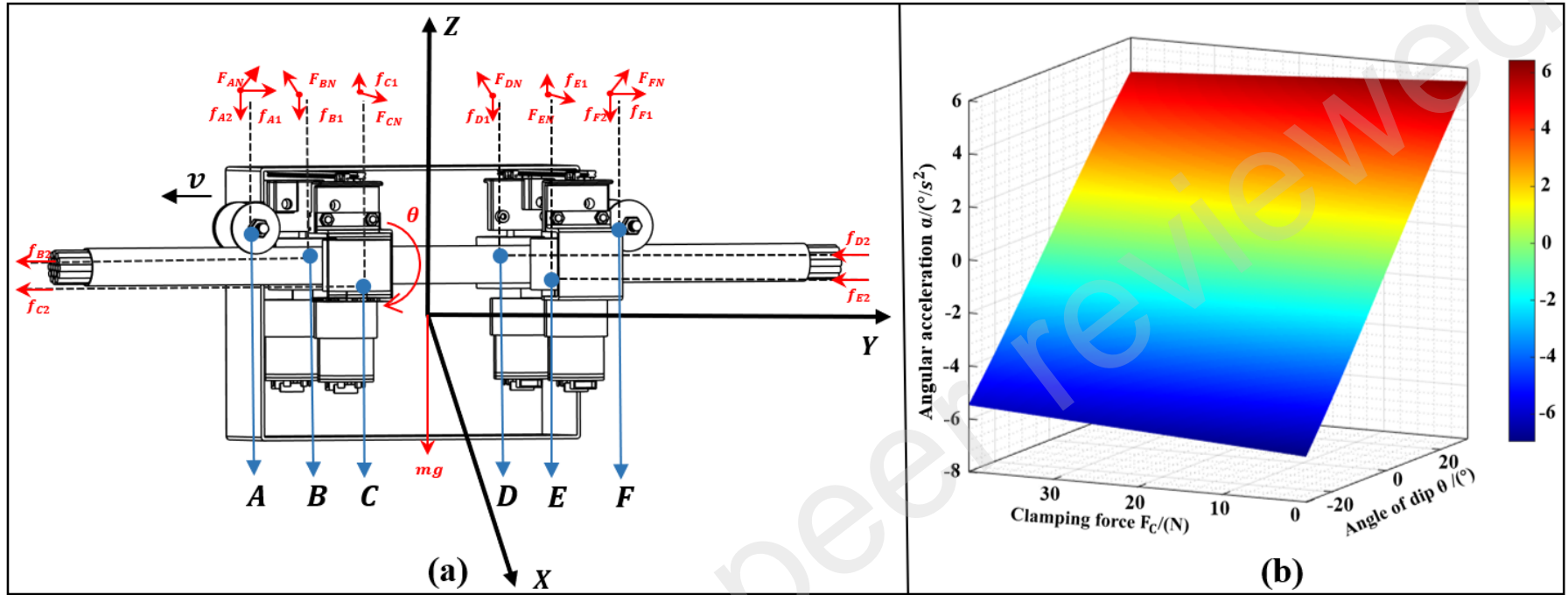


Figure 4. The impact of straight cables on the robot's motion stability: (a) analysis of the forces on the robot. (b) result analysis

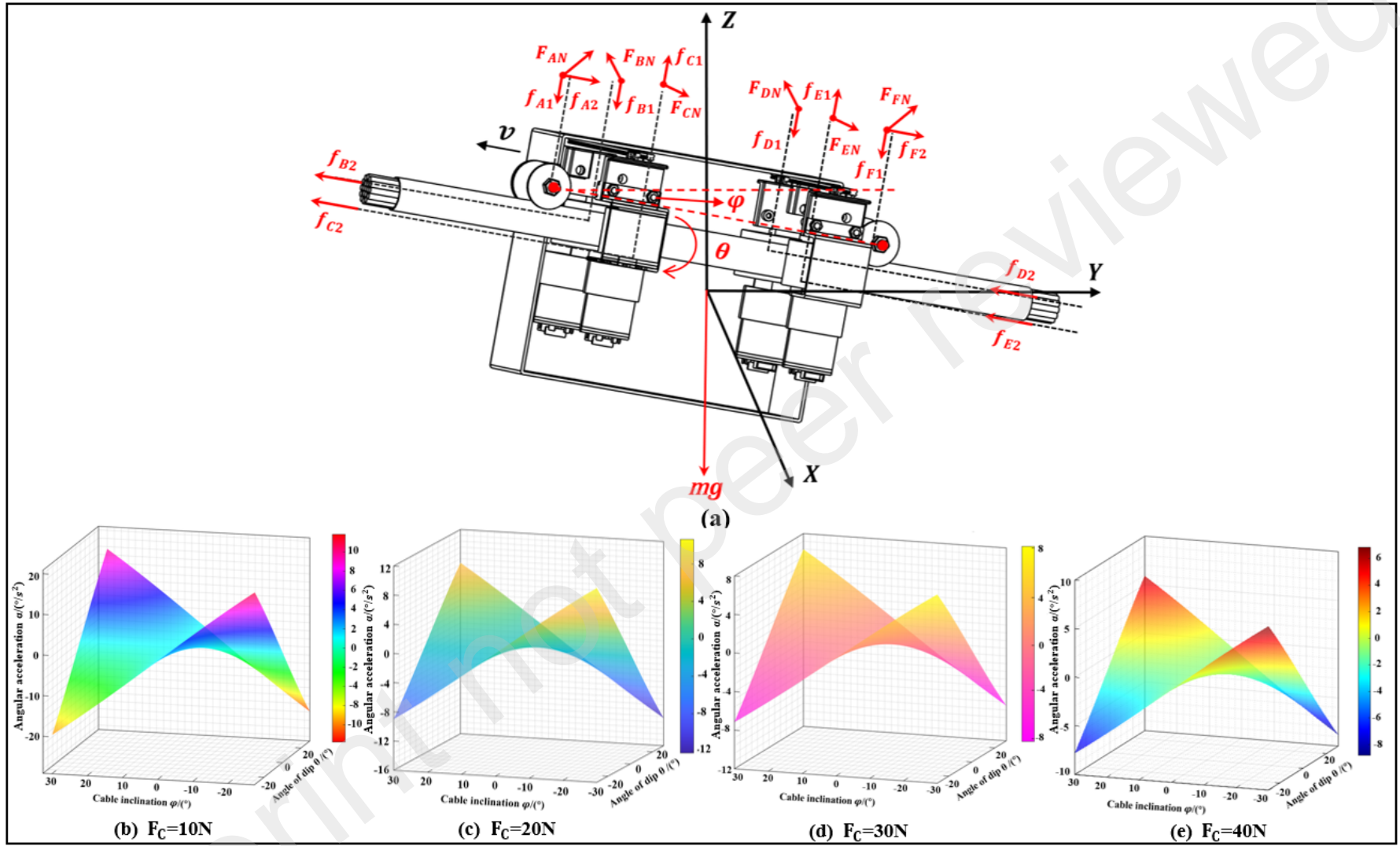


Figure 5. The impact of inclined cables on the robot's motion stability: (a) analysis of the forces on the robot. (b)-(e) results analysis

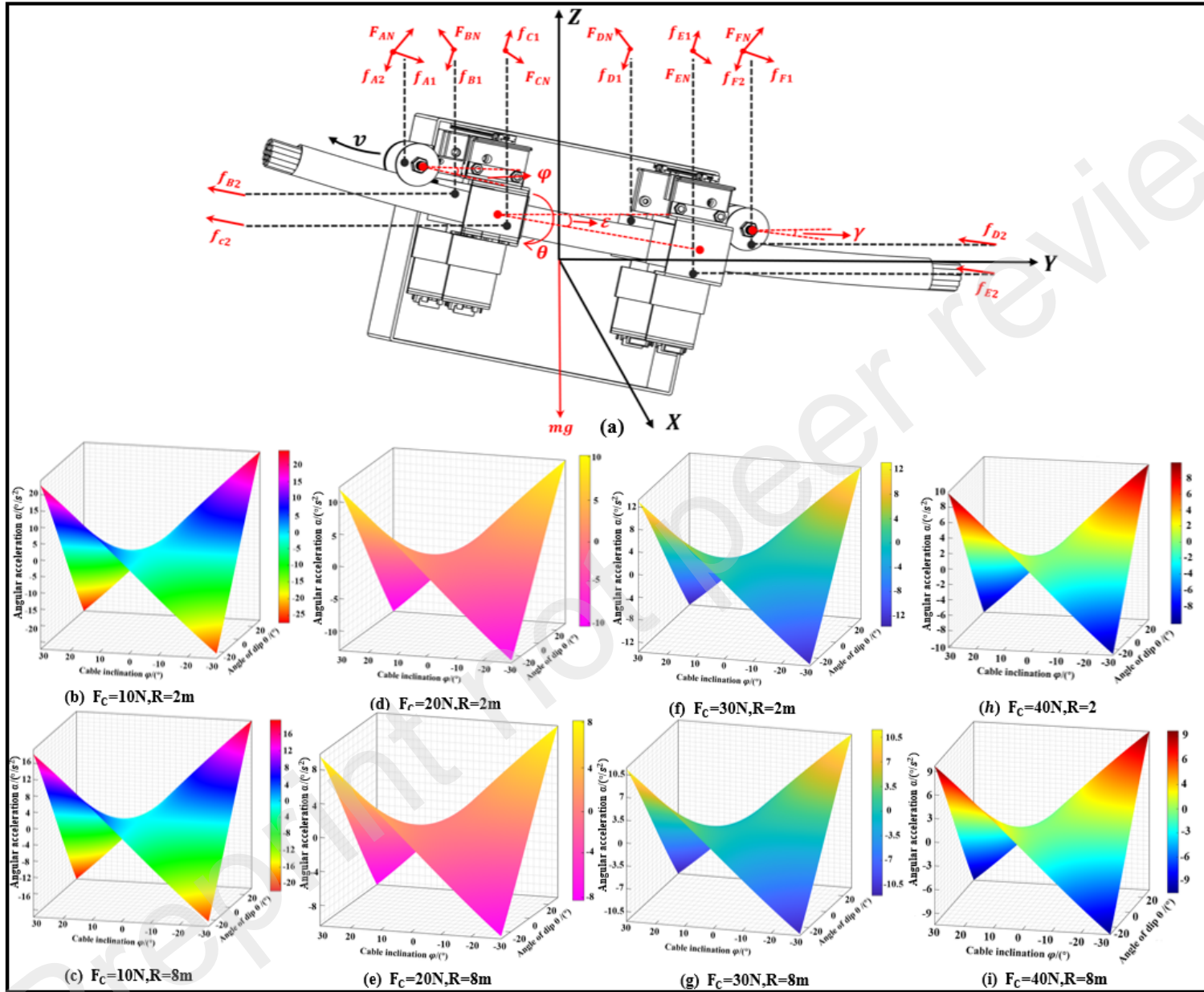


Figure 6. The impact of inclined cables on the robot's motion stability: (a) analysis of the forces on the robot. (b)-(i) results analysis

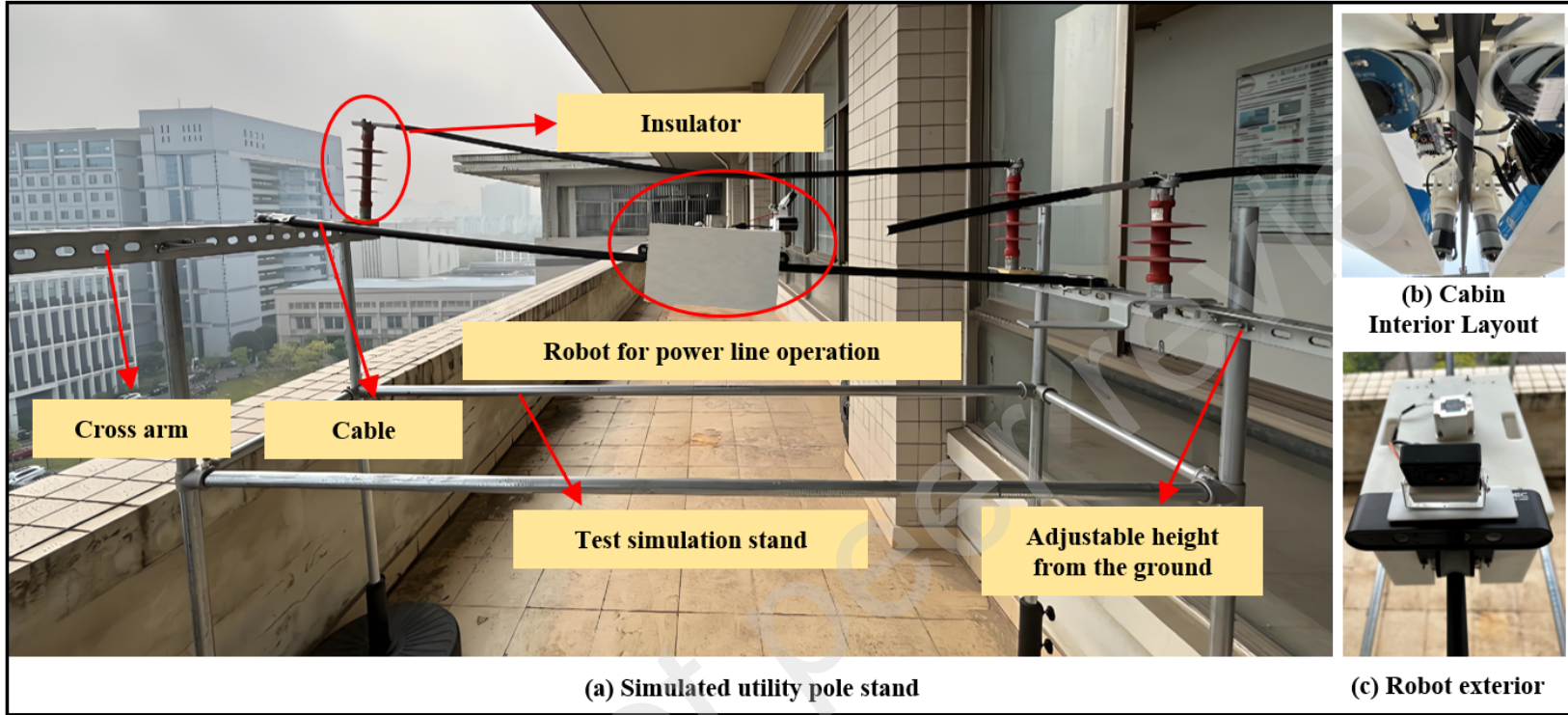
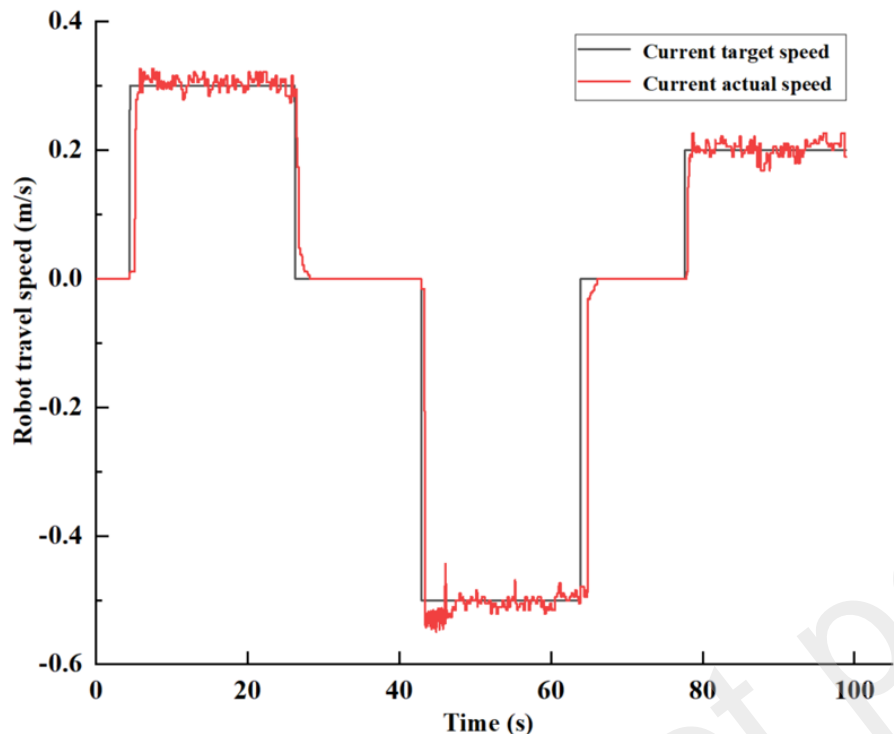
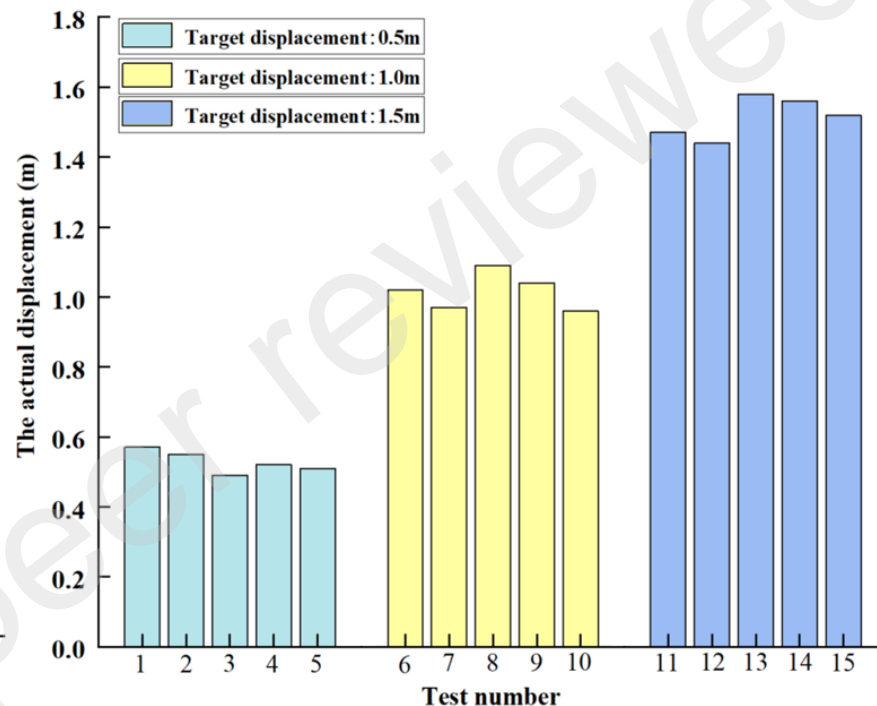


Figure 7. Test scenario: (a)the simulation electric pole test bench. (b)cabin interior layout. (c)robot exterior.



(a)



(b)

Figure 8. The test results on robotic motion control performance: (a) speed control test. (b) displacement control test.

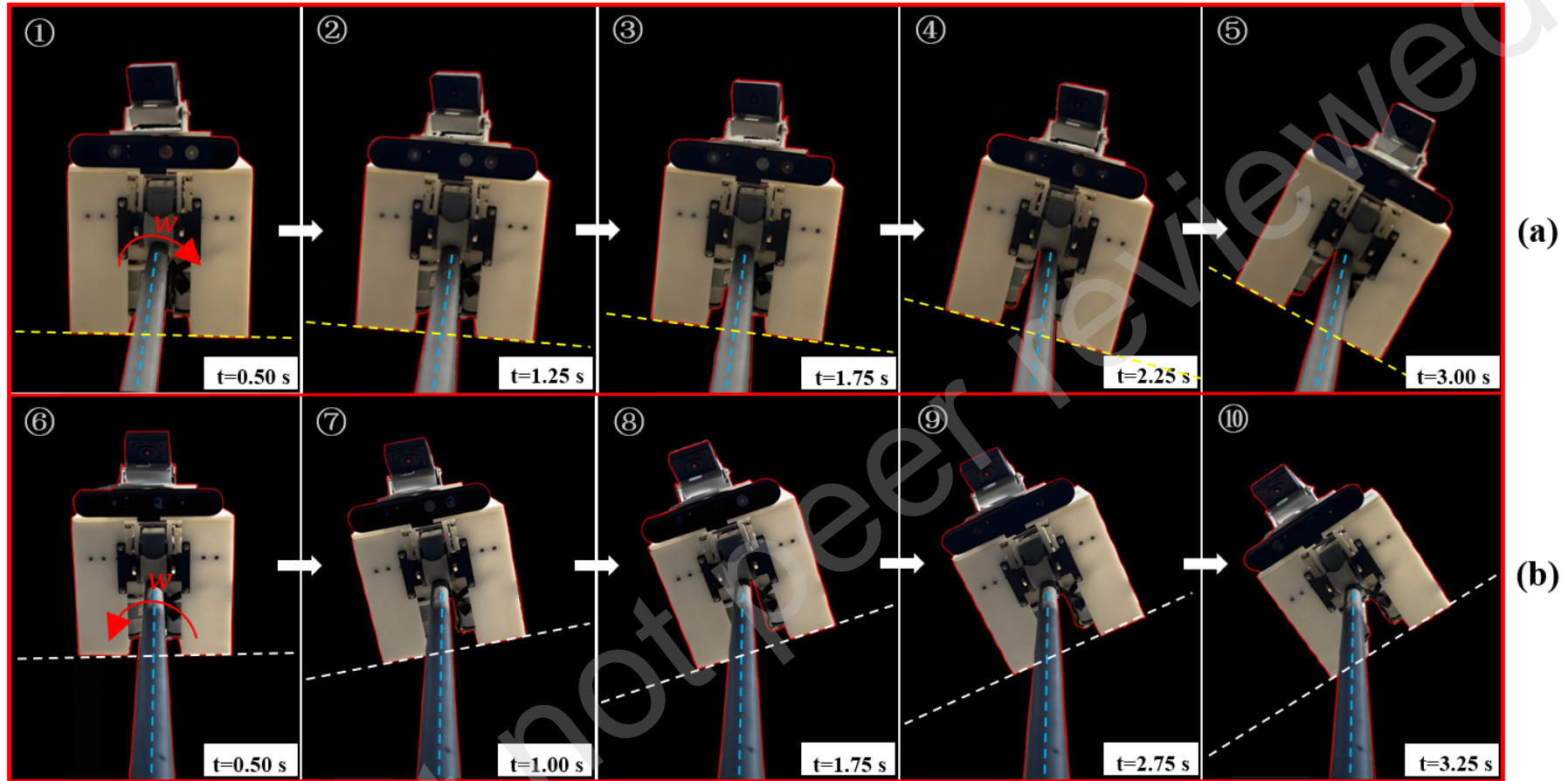


Figure 9. Robot posture.

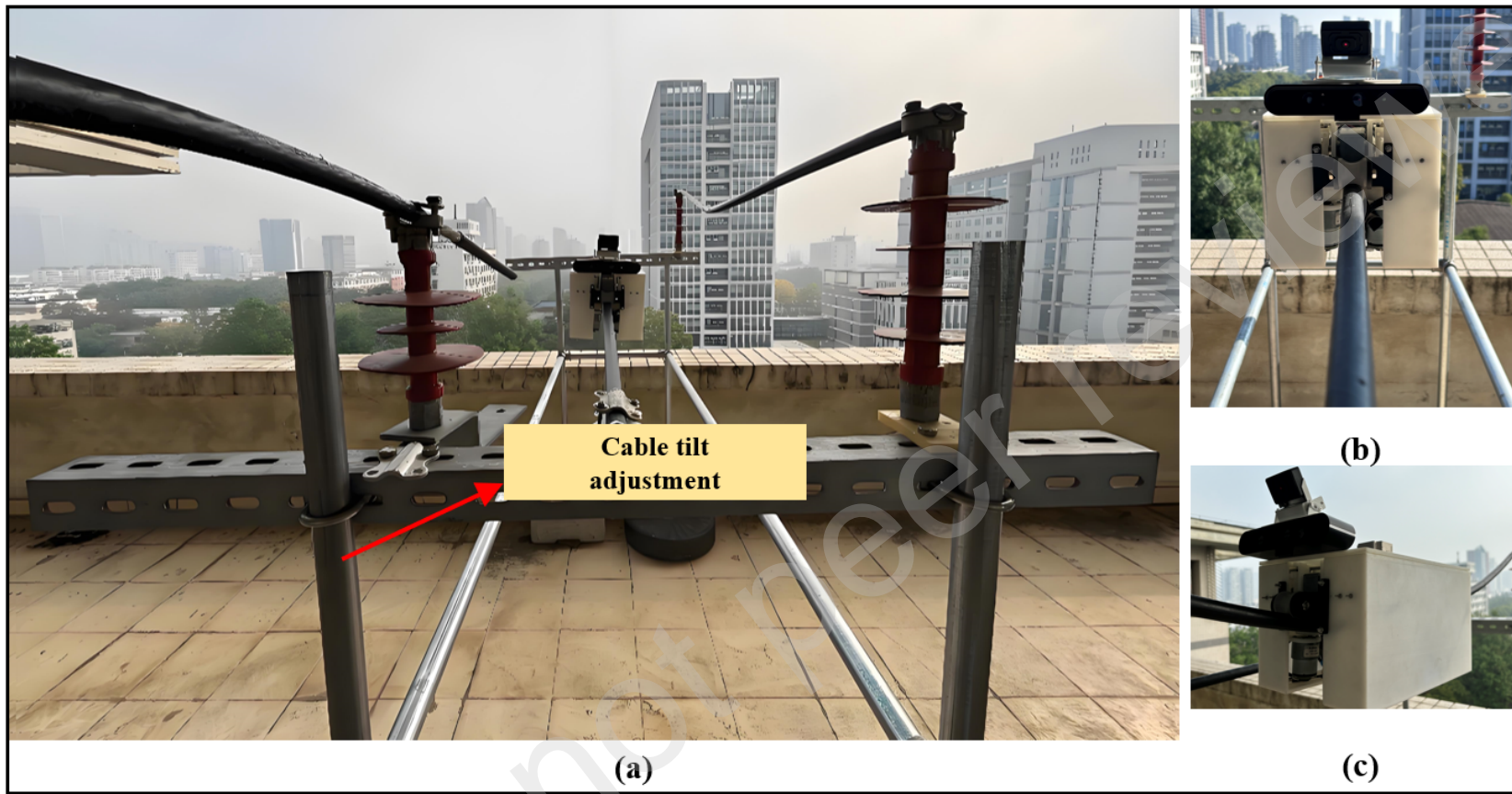


Figure 10. Robot motion stability performance test scenario: (a)inclined cable. (b)straight line cable. (c) suspended chain state cable.

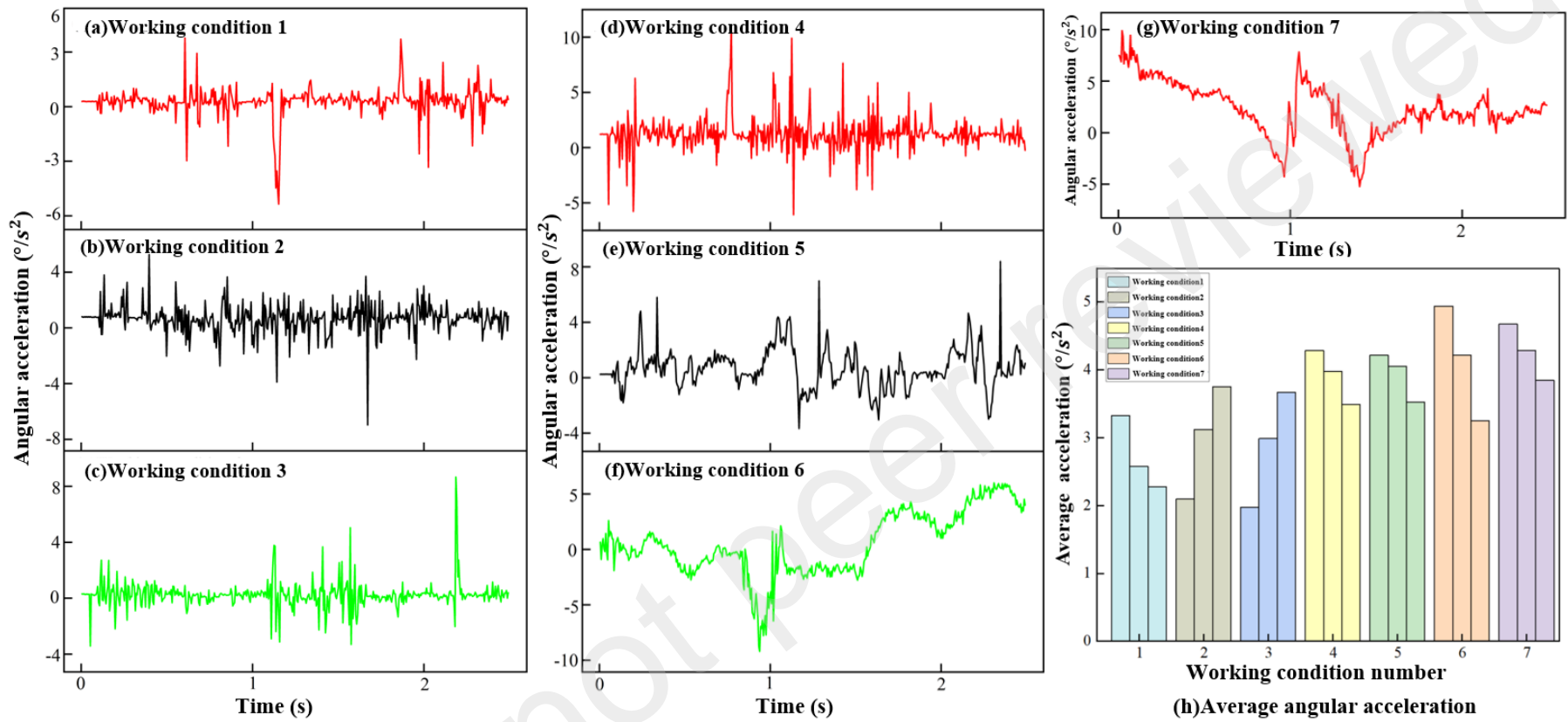


Figure 11. The results of the robot motion stability performance test.

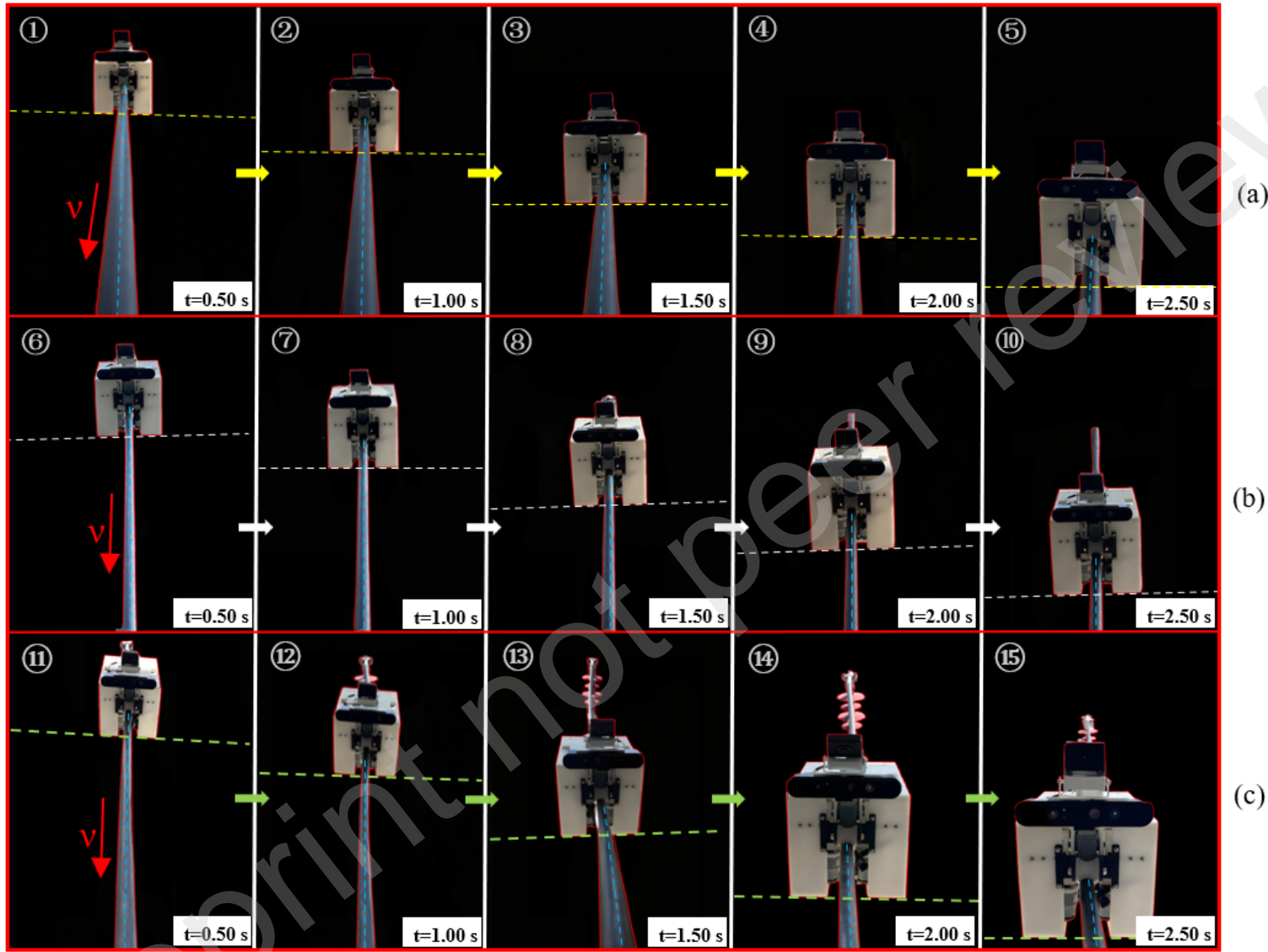


Figure 12. Robot motion posture: (a) robot in straight line cable. (b) robot in inclined cable. (c) robot in suspended chain state cable.